Hydrogen-microvoid interactions at continuum scale

Haiyang Yu[a], Jim Stian Olsen[a], Jianying He[a], Zhiliang Zhang[a,*]

[a]*Department of Structural Engineering, Norwegian University of Science and Technology, 7491 Trondheim, Norway*

Abstract

Experimentally, it has been shown that hydrogen can either enhance the internal necking failure or induce internal shearing failure of microvoids. In this study, the numerical investigation of hydrogen-microvoid interactions under the framework of hydrogen enhanced localized plasticity mechanism reveals that the actual effect of hydrogen depends on the stress state as well as on the hydrogen trapping effect. Hydrogen enhanced internal necking failure is observed over the entire stress space at a low level of trapping effect. While such failure is still observed in the high triaxiality regime at a high level of trapping effect, hydrogen induced internal shearing failure is observed in the low triaxiality regime. A hydrogen induced internal shearing failure criterion is proposed, and the failure loci corresponding to the low and high levels of trapping effect are constructed. The hydrogen induced internal shearing failure locus is found to be approximately independent of stress triaxiality while the hydrogen enhanced internal necking failure locus maintains similar triaxiality dependency as in the absence of hydrogen. The loss of ductility, in terms of reduction in failure strain and dimple size, is more pronounced in the case of hydrogen induced internal shearing failure. Subsequent study of the Lode effect reveals that plane strain tension is the most critical case for hydrogen induced internal shearing failure while axisymmetric tension is the most critical for hydrogen enhanced internal necking failure.

Keywords: hydrogen-microvoid interaction; hydrogen enhanced localized plasticity; internal necking failure; internal shearing failure; failure loci

*Corresponding author

Email address: zhiliang.zhang@ntnu.no (Zhiliang Zhang)

Nomenclature

$\boldsymbol{F^b}$	deformation gradient tensor inside the shear band
$\boldsymbol{F^o}$	deformation gradient tensor outside the shear band
$\dot{\varepsilon}_p^b$	equivalent plastic strain rate inside the shear band
$\dot{\varepsilon}_p^o$	equivalent plastic strain rate outside the shear band
$\dot{\varepsilon}_p$	equivalent plastic strain rate
η	stress triaxiality
$\overline{V}_h$	partial molar volume of hydrogen
σ_0	initial yield stress without hydrogen
$\sigma_0(c)$	initial yield stress with hydrogen
σ_f	flow stress
σ_h	hydrostatic stress
θ_L	fraction of occupied interstitial lattice sites
θ_T	fraction of occupied interstitial trapping sites
ε_e	the effective strain of the unit cell
ε_f	the effective failure strain of the unit cell
$\xi\sigma_0$	initial yield stress at c_L^0
$\zeta\sigma_0$	lower bound of initial yield stress
c	total hydrogen concentration
c_L	lattice hydrogen concentration
c_L^0	initial lattice hydrogen concentration
c_T	trapped hydrogen concentration
D_L	lattice diffusivity coefficient
E_b	trap binding energy
f_0	initial void volume fraction
$HEDE$	hydrogen enhanced decohesion
$HELP$	hydrogen enhanced localized plasticity
k	steepness parameter of the sigmoidal law
K_T	trap equilibrium constant
L	Lode parameter
$M1$	material with low trapping effect
$M2$	material with medium trapping effect
$M3$	material with high trapping effect
n	strain hardening exponent
N_L	lattice site density
N_T	trapping site density
N_T^{exp}	trapping site density fitted from experimental data
x	(normalized) hydrogen concentration in the sigmoidal law
x_0	position parameter of the sigmoidal law

1. Introduction

Hydrogen induced premature failure in steels is a well recognized problem [1, 2], however, its underlying mechanism is still controversial. Popular theories in the hydrogen community include the hydrogen enhanced decohesion (HEDE) mechanism, the hydrogen enhanced localized plasticity (HELP) mechanism and the adsorption-induced dislocation emission (AIDE) mechanism. The HEDE mechanism assumes that dissolved hydrogen reduces the cohesive strength of the iron lattice [3], the HELP mechanism assumes that solute hydrogen enhances dislocation mobility leading to plastic softening [4], and the AIDE mechanism assumes that adsorbed hydrogen promotes dislocation nucleation from crack tips thereby facilitating micro-crack link-up in front of the crack tip[5]. Among these theories, the former two have been adopted in continuum level

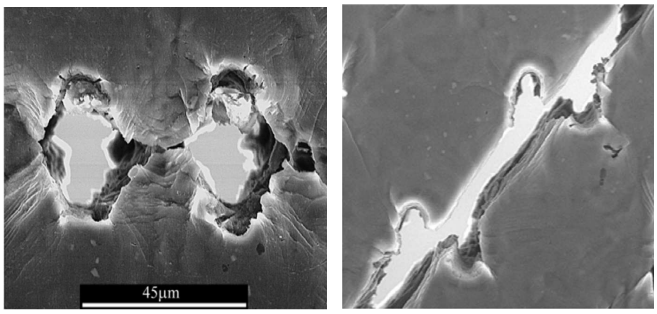

Fig. 1 Illustrations of (*a*) the internal necking failure and (*b*) the internal shearing failure, both taken from Weck and Wilkinson [13].

study of hydrogen induced failure [6, 7]. Compared with HEDE, the HELP mechanism seems to be supported by more direct experimental evidence [4, 8, 9], however, it is not as widely adopted in engineering failure assessment as HEDE. Due to the phenomenological manner, the HEDE mechanism can be readily incorporated into a fracture assessment tool such as the cohesive zone modeling approach [6]; The successful engineering utilization of the HELP mechanism, in contrast, requires a sophisticated understanding of the hydrogen effects on ductile failure mechanism as a premise, which has yet to be achieved.

The ductile failure mechanism is often attributed to the microvoid process which typically involves void nucleation, growth and coalescence [10]. Failure is often characterized by void coalescence [11], and Pineau et al. [12] in their recent review paper categorized this phenomenon into three modes: coalescence by internal necking of the intervoid ligament, by the internal shearing of the matrix and by link-up along the length of voids. Among all these modes, the first and the second are most relevant to the current work, and they are termed hereinafter internal necking failure and internal shearing failure, respectively. As illustrated in Fig. 1, the internal necking failure is often characterized by two sufficiently developed voids with ligaments linking up in between, while the internal shearing failure is characterized by two insufficiently developed voids diagonally linking up through a broken shear band. Within the framework of the HELP mechanism, hydrogen plays a role in the microvoid process by inducing matrix material softening, which could accelerate the void coalescence or even change the failure mode. Experimental study on this aspect has been reported in the literature. Garber et al. [14] performed tensile tests on hydrogen

charged and uncharged round bar specimens made from two different lab heats of a near-eutectoid steel and found that hydrogen increased the dimple size at failure in both cases. Therefore, they claimed that hydrogen promoted void growth and coalescence in these materials. Later, Garber et al. [15] performed similar experiments on a higher carbon steel AISI 1080 and a lower carbon steel AISI 1018. In the AISI 1080 steel, increased dimple size at failure was found in the presence of hydrogen, indicating that hydrogen promoted void growth during the link-up stage; in the AISI 1018 steel, however, decreased dimple size was observed in hydrogen charged specimens, and this was attributed to the hydrogen promoted unstable shearing of the matrix at a lower void volume fraction. Therefore, hydrogen could enhance either the internal necking failure mode or the internal shearing failure mode, which is dependent on the material. Cialone and Asaro [16] performed tensile tests with hydrogen on plain carbon steels and found that hydrogen enhanced the internal necking failure mode. Recently, Matsuo et al. [17] performed axisymmetric tensile tests with hydrogen on the pipeline steel JIS-SGP. Longitudinal growth of microvoids parallel to the tensile axis was observed in uncharged specimens while obvious lateral void growth leading to earlier coalescence was observed in hydrogen charged specimens, which indicated hydrogen enhanced necking failure. Meanwhile, substantial experimental evidence for hydrogen induced internal shearing failure exists in the literature. Lee et al. [18, 19] reported hydrogen enhanced plastic instability along characteristic slip paths in AISI 1090 and AISI 1095 steels. Onyewuenyi and Hirth [20], Yunchang and Koss [21], Somerday et al. [22] reported accelerated shear instability process due to hydrogen in the AISI 1090 steel, Zirconium alloy and duplex stainless steel. More relevantly, Park and Thompson [23] performed axisymmetric tensile tests on hydrogen charged specimens made from AISI 1520 steel. Microvoid link-up by localized shearing, quite similar to that shown in Fig. 1(b), was observed at the central crack initiation site; in addition, the dimple size at failure was not significantly changed with hydrogen. In contrast, internal necking failure similar to that shown in Fig. 1(a) was observed in tensile tests on the same material in the absence of hydrogen [24]. Therefore, the authors concluded that hydrogen changed the failure mode from internal necking in the absence of hydrogen to internal shearing in the presence of hydrogen. Most recently, Matsuo et al. [25] performed axisymmetric tensile tests on hydrogen charged specimens made from Type 316L stainless steel. In contrast to the experiments on pipeline steel JIS-SGP reported by the

same authors [17], reduced average size of dimples at failure was observed, indicating no hydrogen enhanced lateral void growth. These authors therefore concluded that hydrogen accelerated the formation of void sheets by inducing localization of shear deformation, i.e. induced internal shearing failure in Type 316L stainless steel.

Numerical investigation on the hydrogen effects on ductile failure mechanism has also been reported. Sofronis et al. [7], Liang et al. [26] studied hydrogen induced shear localization in plane strain tensile specimens using a coupled hydrogen-plasticity approach through HELP mechanism. Shear bands were successfully generated in their numerical simulations, and they concluded based on the shear bifurcation criterion proposed by Rudnicki and Rice [27] that hydrogen induced material softening caused the critical modulus for shear bifurcation to become positive thereby leading to shear band formation which is otherwise impossible. Liang et al. [26], in addition, discussed the hydrogen facilitated necking in the plain strain tensile specimen. Barrera et al. [28] studied the effects of hydrogen induced material softening on a plate with a deep notch. In their work, hydrogen diffusion and the mechanical behavior were coupled via a different approach from that used by Liang et al. [26]. Direct investigation on hydrogen-microvoid interaction also exists in the literature. Premono et al. [29] studied the hydrogen induced material softening effects on a void-containing material volume whose boundary conditions are determined by the displacement field at the center of a tensile specimen, and they found that hydrogen assisted void growth. The same authors [30] studied the hydrogen softening effects on the behaviors of square and diagonal void arrays and found that the hydrogen effect seemed to be the strongest on internal necking failure. A more sophisticated approach to investigate the hydrogen-microvoid interaction is the unit cell analysis. The unit cell approach, pioneered by Koplik and Needleman [31], is an ideal tool for study of ductile failure mechanism featured by microvoid process. The subject of analysis is a void-containing representative material volume with periodic boundary conditions to reflect the interaction with neighbouring cells. Within this framework, the ductile failure mechanism under a proportional loading path or a specially designed non-proportional loading path can be studied in a straightforward manner. For a detailed introduction to this approach, the readers are referred to Yu et al. [32]. Utilizing the unit cell approach, Ahn et al. [33] investigated hydrogen-induced plastic flow localization during void growth and coalescence with material data relevant to

A533B steel. At a medium stress triaxiality of $\eta = 1.0$, hydrogen induced shear band activity was observed; at a high stress triaxiality of $\eta = 3.0$, hydrogen enhanced internal necking failure took place. In a similar manner, Liang et al. [34] studied the effects of hydrogen trapping on void growth and coalescence with material data relevant to a niobium system, where only reversible hydrogen trapping sites at dislocations were considered. It was observed that hydrogen could enhance void link-up at medium triaxialities; however, such effect was negligible if the trap density is too small or if the stress triaxiality is too large. In these studies, the development of hydrogen induced shear band was phenomenologically described and explained, however, the actual effect of the shear band on the failure mechanism was not treated properly. In Ahn et al. [33], for instance, the internal shearing failure mode was not defined, and failure in the presence of shear band was still detected with the inter-ligament necking coalescence criterion [31], which yielded delayed failure point and a large void volume fraction at failure. These unit cell studies on hydrogen-microvoid interactions are all performed with an existing microvoid. In reality, void nucleation from precipitates and inclusions is also an important stage in hydrogen induced failure, which can be accounted for by inserting a hard particle into the unit cell and modelling the interface with cohesive zone approach [35, 36]. This procedure, however, requires additional parameters reflecting the hydrogen induced degradation of cohesive properties and has limited influence on the microvoid failure mode, therefore, it is not considered in the present work.

The common feature of all the numerical studies reviewed in the previous paragraph is that a linear degradation of the yield stress and a constant strain hardening exponent with an increasing hydrogen concentration are assumed to reflect the hydrogen induced softening effect on the matrix material, which is adopted in view of the absence of any conclusive experimental evidence about the hydrogen effect on the strain hardening exponent [26]. While the linear hydrogen softening law is a wise option due to its simplicity, it could cause certain limitation to the unit cell studies by Ahn et al. [33], Liang et al. [34]. To the best of our knowledge, these studies are the first attempts to study the hydrogen effect on microvoid growth and coalescence directly, and they seem to be the only ones by far. While the simulations were successful and the conclusions logical, we note that the stress triaxiality regime investigated by these studies was $1 \leq \eta \leq 3$, which represents the range of blunt notched specimens and crack tip fields [34]. The regime of $\eta \leq 1$, however,

is inadequately explored, and the reason might be that no significant hydrogen effect on void growth and coalescence can be observed at small triaxiality with the linear softening law, even if a severe hydrogen induced softening effect is assumed [34]. In this sense, the unit cell results are not directly comparable to the aforementioned experiments that were performed on axisymmetric smooth tensile specimens where the typical stress triaxility at necking is $0.6 \leq \eta \leq 0.8$. We will show later that the change from longitudinal to lateral void growth observed by Matsuo et al. [17] in axisymmetric tensile tests with hydrogen cannot be captured by unit cell analysis with the linear hydrogen softening law, however severe the softening effect is. In order to match the experimental observations in the low triaxiality regime, a different form of hydrogen softening law is proposed in this work.

While the shear bifurcation criterion [27] was successfully implemented by Sofronis et al. [7], Liang et al. [26] to the plane strain tensile specimens, it is not directly applicable to the unit cell analysis. Therefore, a criterion for failure due to internal shearing of voids is still lacking, and hence the hydrogen induced shear localization can only be illustrated phenomenologically and discussed qualitatively, as done by Ahn et al. [33], Liang et al. [34]. For the sake of engineering failure assessment, it is beneficial to determine a failure locus, which can be easily done for the internal necking failure using the void coalescence criterion proposed by Koplik and Needleman [31] but is not possible for the case of internal shearing failure due to the lack of a proper internal shearing failure criterion for microvoids. Extensive work on shearing failure of microvoids has been done using the unit cell approach. Dunand and Mohr [37] performed 3D unit cell analyses with a shearing component. Failure was detected when the localization of deformation into a narrow planar band occurred, and the criterion proposed by Needleman and Tvergaard [38] was applied. Similar procedure and failure criterion were adopted by Barsoum and Faleskog [39, 40]. Tvergaard [41], on the other hand, performed direct bifurcation analysis to determine the point of localization into a shear band. A common feature of these studies is that the width of the shear band is much larger than the void spacing inside the band [41], therefore, microvoids could spin as well as grow during loading. The case of hydrogen induced internal shearing failure treated in the present work, however, is different in that it belongs to another category of void shearing where the shear band width is smaller than the unit cell size [12]. As observed by Ahn et al. [33], Liang et al.

[34] and to be elaborated later by us, the hydrogen induced shear band emanates from the void surface and propagates to the cell boundary, and it is quite narrow and causes no void spinning. For such scenario, a new criterion for internal shearing failure is proposed based on the definition of shear localization, and it will be shown that this criterion, in the plane strain case, is equivalent to that adopted by Li and Wierzbicki [42].

Thanks to the newly proposed internal shearing failure criterion, the hydrogen failure loci in both 2D and 3D scenarios are constructed, and the parametric study on a variety of factors including hydrogen trapping effect, hydrogen softening effect and initial void volume fraction is performed. This article is organized as follows: the modeling framework, the hydrogen softening law and the internal shearing failure criterion are presented in section 2; the results and discussion regarding the hydrogen failure loci are elaborated in section 3; a summary is given in section 4. Detailed verification of the internal shearing failure criterion are presented in Appendix A and Appendix B.

2. Formulation and methodology

Hydrogen-microvoid interaction is studied using fully coupled hydrogen diffusion-mechanical analysis within the framework of the HELP mechanism. The microvoid behavior is simulated via the unit cell approach.

Following Ahn et al. [33], Liang et al. [34], the HELP mechanism is reflected at the continuum level as hydrogen induced plastic softening, more specifically, hydrogen lowers the initial yield stress while keeping the strain hardening exponent constant. Throughout this work, J2 flow theory with isotropic hardening is applied to describe the plastic flow in the matrix material

$$\sigma_f = \sigma_0(c)(1 + \frac{\varepsilon_p}{\varepsilon_0})^n \tag{1}$$

where σ_f is the flow stress, $\sigma_0(c)$ the initial yield stress which is a function of the total hydrogen concentration c, ε_p the plastic strain and $\varepsilon_0 = \sigma_0(c)/E$ the corresponding yield strain with E being the Young's modulus. The hydrogen induced softening as described by this equation is implemented via the UHARD user subroutine in ABAQUS [43].

Apparently, the total hydrogen concentration c is important for determining the initial yield stress at any time. In the present work, the total hydrogen population is assumed to be comprised of two communities, the lattice hydrogen residing at normal interstitial lattice sites and the trapped hydrogen residing at dislocation traps [34], namely

$$c = c_L + c_T \tag{2}$$

where c_L is the lattice hydrogen concentration and c_T the trapped hydrogen concentration. These two quantities can be further expressed as

$$c_L = \theta_L N_L \qquad\qquad c_T = \theta_T N_T \tag{3}$$

where θ_L is the fraction of occupied interstitial lattice sites and N_L the lattice site density, i.e. the number of lattice sites per unit volume; similarly, θ_T is the fraction of occupied trapping sites and N_T the trapping site density.

The hydrogen concentration is determined by the diffusion analysis with the governing equation proposed by Sofronis and McMeeking [44]

$$\frac{\partial c_L}{\partial t} + \frac{\partial c_T}{\partial t} - \nabla \cdot (D_L \nabla c_L) + \nabla \cdot (\frac{D_L c_L \overline{V}_h}{RT} \nabla \sigma_h) = 0 \tag{4}$$

where D_L stands for the lattice diffusivity coefficient, $\overline{V}_h$ the partial molar volume of hydrogen, σ_h the hydrostatic stress, R the universal gas constant and T the absolute temperature.

Oriani [45] assumed an equilibrium between hydrogen in lattice sites and in trapping sites

$$\frac{\theta_T}{1 - \theta_T} = \frac{\theta_L}{1 - \theta_L} K_T \tag{5}$$

where K_T is the trap equilibrium constant $K_T = exp(-E_b/RT)$ with E_b being the trap binding energy which is inherently negative. Through the equilibrium condition, the relation between the

lattice and trapped hydrogen concentration is derived

$$c_T = \frac{N_T}{1 + \frac{1}{K_T \theta_L}} \qquad \frac{\partial c_T}{\partial c_L} = \frac{c_T(1-\theta_T)}{c_L} \tag{6}$$

Following Eqs.(3-6), we are able to determine the hydrogen concentration during the loading process by analogizing the transient hydrogen diffusion to heat transfer analysis, via the UMATHT user subroutine in ABAQUS [46]. The fully coupled hydrogen-plasticity interaction through HELP mechanism is then realized by incorporating the UMATHT user subroutine for hydrogen diffusion and the aforementioned UHARD user subroutine for hydrogen induced softening into a coupled temperature-displacement analysis procedure. Considering that slow strain rate loading condition is adopted in this work, the current approach is equivalent to the steady state solution based approach employed by Liang et al. [34]. Moreover, it can be readily applied, due to the transient nature of hydrogen diffusion analysis, to study the loading rate effect which is a direction of our further work.

The unit cell approach is employed here to investigate the behavior of an individual microvoid taken from a periodic array of microvoids, in both 2D and 3D situations. Periodic displacement boundary conditions are applied to the boundaries of the unit cell, and the loading path is assumed to be proportional. To represent a material point taken from a hydrogen pre-charged specimen, initial uniform hydrogen concentration c_0 is applied throughout the cell and insulated hydrogen boundary conditions are applied to the cell boundaries as well as to the void surface. The initial void volume fraction of the unit cell is $f_0 = 0.001$ for both the 2D and 3D cases. Illustrations of the 2D and 3D unit cells are given in Fig. 2. In the present work, the stress triaxiality η and the Lode parameter L are utilized to characterize the stress state on the unit cell

$$\eta = \frac{-p}{q} \tag{7}$$

$$L = \frac{2\sigma_2 - \sigma_1 - \sigma_3}{\sigma_1 - \sigma_3} \tag{8}$$

where p and q are the hydrostatic pressure and the equivalent stress, respectively; σ_1, σ_2 and σ_3

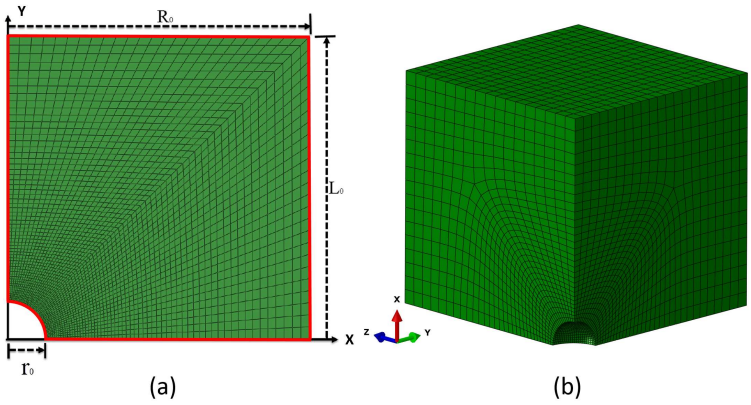

Fig. 2 Illustration of the unit cells with an initial void volume fraction of $f_0 = 0.001$: (a) the 2D situation with only a quarter of the cell shown due to axisymmetry and (b) the 3D situation with only one eighth of the cell shown due to symmetry. The red line represents the insulated boundary conditions for hydrogen diffusion.

are the three principal stress components arranged in the sequence of $\sigma_1 > \sigma_2 > \sigma_3$. The stress triaxiality indicates the level of constraint, and the Lode parameter determines the specific position of the stress point on the deviatoric plane, for instance, the stress state with $\eta = 1.0$ and $L = -1.0$ is relevant to an axisymmetric notched tensile bar and that with $\eta = 1.0$ and $L = 0$ to a plane strain notched tensile specimen. More details regarding the stress state characterization can be found in Yu et al. [32].

2.1. Material properties

Considering the complexity in material microstructures and hydrogen trapping sites in reality, we do not target a specific material. Instead, we consider dislocation as the only type of hydrogen trapping site and perform comparative study among three specially tailored materials representative of low, medium and high levels of hydrogen trapping effect. For these materials, the trap binding energy is kept the same and the difference in hydrogen trapping effect is reflected by the variation in trap density, which is acceptable considering that it is the overall hydrogen trapping effect that influences the mechanical behavior of the microvoids under the current modeling framework. The trap binding energy is selected as a low value, conforming to the findings from Novak et al. [47] and Ayas et al. [48], which indicated that the only possible trapping sites associated with hydrogen induced fracture were low binding energy dislocations [46]. In addition, a realistic

material is adopted in order to relate the numerical results qualitatively to experimental evidence.

The focus of this work is the parametric study of the microvoid behavior with different levels of hydrogen trapping and softening effects, therefore, the mechanical properties in the absence of hydrogen are assumed to be the same for all the materials. J2 flow theory with isotropic hardening is applied to describe the plastic behavior of the matrix material, as given by Eq.(1), with the hydrogen unaffected initial yield stress $\sigma_0 = 400$ MPa, the Young's modulus $E = 2 \times 10^5$ MPa, the Poisson's ratio $\nu = 0.3$ and the strain hardening exponent $n = 0.1$.

The lattice site density is assumed as $N_L = 8.74 \times 10^{19}$ sites/mm^3 and the partial molar volume of hydrogen as $\overline{V}_h = 2 \times 10^3$ mm^3/mol,which are kept the same for all the materials. The hydrogen diffusion coefficient has no influence on the results and is not specified, since the loading rate in this work is sufficiently slow for hydrogen diffusion to reach the steady state. Therefore, the total hydrogen concentration and consequently the mechanical behavior of the microvoids are completely controlled by the two remaining parameters, the trap site density N_T and the trap binding energy E_b. These two parameters influence the hydrogen-microvoid interaction through their combined effect on the proportion of trapped hydrogen in the total concentration. Both Ahn et al. [33] and Liang et al. [34] implied that the failure mode of the microvoid tended to change from the hydrogen enhanced internal necking to hydrogen induced internal shearing as the trapping effect became important. In order to study all the possible failure modes in the presence of hydrogen, the three specially tailored materials has to cover a sufficiently wide range of trapping effects. A summary on the trapping site density N_T and the trap binding energy E_b was recently given by Jemblie et al. [46]. N_T is related to the plastic deformation scaled by the equivalent plastic strain ε_p, and it can be expressed as a function of ε_p as proposed in Sofronis and McMeeking [44] by extrapolating the experimental data reported by Kumnick and Johnson [49]

$$log N_T^{exp} = 23.26 - 2.33 exp(-5.5\varepsilon_p) \tag{9}$$

with N_T^{exp} denoting the trapping site density obtained based on experimental data. Alternatively, a theoretical approach, which related N_T to the dislocation density, was proposed by Sofronis et al. [7]. It was shown by Jemblie et al. [46] that the latter approach yielded a dislocation trap density

2 to 3 orders of magnitude larger than N_T^{exp}. We therefore assume that the value of dislocation trap density falls in the range $(N_T^{exp}, 1000N_T^{exp})$. Following Yagodzinskyy et al. [50], we set the same trap binding energy $E_b = -15.4$ kJ/mol for three materials $M1$-$M3$ and attribute different trap densities, N_T^{exp}, $200N_T^{exp}$ and $500N_T^{exp}$, to them, yielding three levels of overall hydrogen trapping effect: $M1$ represents a low level of hydrogen trapping effect, $M2$ a medium level of hydrogen trapping effect and $M3$ a high level of hydrogen trapping effect. These parameters are determined based on a preliminary case study which shows a transition of the failure mode from internal necking with $M1$ to internal shearing with $M2$. It is further noticed that materials $M2$ and $M3$ could be related qualitatively to the fcc austenitic steels in terms of dislocation trapping characteristics [51]. Material $M1$, however, should be viewed as an artificial material system other than iron, which is designed to yield a very low level of hydrogen trapping effect; as will be shown later, this material leads to hydrogen enhanced internal necking failure mode, somewhat similar to the scenario observed by Liang et al. [34] in the niobium system. In order to relate our numerical results not only to the experimental evidence reported on the Type 316L stainless steel [25], but also to that on the JIS-SGP steel [17], we add an additional material $M4$ using the experimentally obtained trapping parameters on a bcc steel [44], i.e. $N_T = N_T^{exp}$ and $E_b = -60.0$ kJ/mol. A summary of the hydrogen related parameters for all the materials used in the present work is given in Table 1.

Table 1 Material properties of the four model materials.

Material	*Dislocation trap density*	*Trap binding energy* (kJ/mol)
$M1$	N_T^{exp}	-15.4
$M2$	$200N_T^{exp}$	-15.4
$M3$	$500N_T^{exp}$	-15.4
$M4$	N_T^{exp}	-60.0

* Material properties not listed here have been given earlier and are identical for all the materials.

2.2. *Hydrogen softening law*

The hydrogen softening law is a critical material property in hydrogen-microvoid interactions. In all the previous studies, this relation has been treated as a linearly decreasing function of c

for simplicity [34]. The linear hydrogen softening law, however, is found unable to account for certain experimental observations. As observed by Matsuo et al. [17] in the JIS-SGP pipeline steel, hydrogen clearly promoted lateral void growth leading to premature failure in the early necking stage of an axisymmetric tensile test. According to our numerical case study on a smooth round tensile bar, the characteristic stress triaxiality at the early stage of necking can be approximated as $\eta \approx 0.7$. We found that no hydrogen enhanced lateral growth of microvoids could be captured at such low stress triaxiality under the framework of a linear hydrogen softening law. Therefore, a new form of the hydrogen softening law needs to be adopted in order to reproduce the experimental observation.

As a first step, we discuss the generic limitation of the linear hydrogen softening law and aim to find a new form which is able to yield hydrogen enhanced lateral void growth results at $\eta \approx 0.7$, without relating the numerical results to the experimental observation on the JIS-SGP pipeline steel [17]. The hydrogen enhanced lateral void growth is realized through hydrogen induced local softening in the ligament between adjacent voids. The hydrogen softening effect have been associated with the total hydrogen concentration in the studies on hydrogen-microvoid interactions so far, which is also adopted in this work. Therefore, the site with the most severe material softening effect is the one with the highest local total hydrogen concentration. It can be easily verified that such site lies on the central ligament (horizontal direction) between the voids in the case where the total hydrogen concentration is dominated by the lattice hydrogen concentration c_L, e.g. material $M1$ with a low level of hydrogen trapping effect; in the case where the proportion of trapped hydrogen c_T in the total concentration becomes significant, however, it lies on a band approximately 45° with respect to the horizontal direction, e.g. material $M3$ with a high level of hydrogen trapping effect. As will be elaborated in subsection 3.1, the former case is the most prone to hydrogen enhanced lateral void growth, especially in the low stress triaxiality regime. Based on these considerations, the artificial material $M1$, which always produces a lattice hydrogen concentration dominant scenario, is selected to model the hydrogen enhanced lateral void growth at $\eta = 0.7$, based on which the limitation of the linear hydrogen softening law is discussed.

While the specific expressions for the linear softening behavior vary from one study to another,

they can be unified into the form utilized by Ahn et al. [33]

$$\sigma_0(c) = \begin{cases} [(\xi - 1)\frac{c}{c_L^0} + 1]\sigma_0 & \sigma_0(c) > \zeta\sigma_0 \\ \zeta\sigma_0 & \sigma_0(c) \leq \zeta\sigma_0 \end{cases} \tag{10}$$

where σ_0 is the initial yield stress at zero hydrogen concentration, $\xi\sigma_0$ the initial yield stress at the initial lattice hydrogen concentration c_L^0 and $\zeta\sigma_0$ the lowest possible value of the yield stress considering that hydrogen cannot cause the yield stress to vanish in reality. Apparently, ξ represents the severity of hydrogen softening effect with a smaller ξ representing a stronger softening effect. Based on this relation, we can get the expression for the maximum level of hydrogen induced softening during the loading of the unit cell. As mentioned, a uniform initial lattice hydrogen concentration c_L^0 is applied to the cell, meaning that the matrix material has an initial yield stress of $\xi\sigma_0$ (Eq.(10)). Assuming that the maximum total hydrogen concentration upon loading is c_{max}, we can obtain the absolute value of the maximum reduction in the initial yield stress as

$$\xi\sigma_0 - \sigma_0(c_{max}) = (1 - \xi)(\frac{c_{max}}{c_L^0} - 1)\sigma_0 \tag{11}$$

and the relative reduction is readily obtained as

$$\frac{\xi\sigma_0 - \sigma_0(c_{max})}{\xi\sigma_0} = (\frac{1}{\xi} - 1)(\frac{c_{max}}{c_L^0} - 1) \tag{12}$$

Both equations are increasing functions of $\frac{c_{max}}{c_L^0}$ and decreasing functions of ξ. Therefore, under the present case of material $M1$ and $\eta = 0.7$, we have higher chance of lateral void growth with a smaller value of ξ, due to larger reduction in the initial yield stress. However, no obvious hydrogen enhanced lateral void growth can be observed in the coupled hydrogen diffusion-unit cell analysis even if we try an unrealistically small value of $\xi = 0.3$ corresponding to a 70% reduction of the initial yield stress at the beginning of calculation, as shown in Fig. 3(b). Negligible influence of hydrogen on the lateral void growth is observed up to the effective strain $\varepsilon_e = 1.601$, compared with Fig. 3(a) which illustrates the growth of the microvoid with no hydrogen. No internal necking

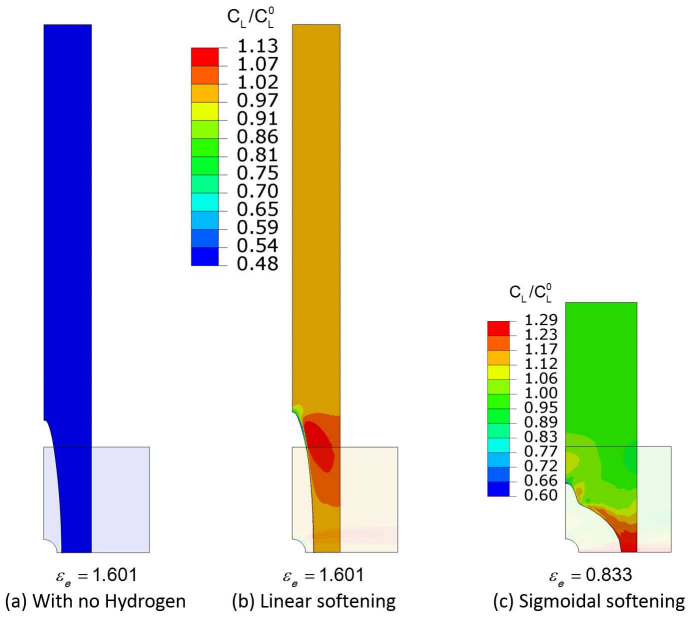

Fig. 3 Comparison of the void growth process modelled by the coupled hydrogen diffusion-unit cell analysis at a low stress triaxiality $\eta = 0.7$: (a) the case without hydrogen at the effective strain $\varepsilon_e = 1.601$; (b) the case with the linear hydrogen softening law with $\xi = 0.3$ at $\varepsilon_e = 1.601$; (c) the case with the sigmoidal hydrogen softening law with $k = 15$ at $\varepsilon_e = 0.833$, note that void coalescence by internal necking is firstly detected at $\varepsilon_e = 0.797$. The transparent part represents the undeformed unit cell.

or shear band formation is observed in both figures. Close observation on Fig. 3(b) reveals that the peak hydrogen concentration c_{max} during loading at such low level of stress triaxiality is not highly distinguished from c_L^0, which, according to Eqs.(11,12), means that the level of softening is acctually very low in spite of the very small value of ξ. Therefore, the linear hydrogen softening law is unable to simulate the experimental observation of hydrogen enhanced lateral void growth in the low stress triaxiality regime.

Intuitively, we can say that the problem discussed in the previous paragraph is caused by application of the same slope of hydrogen softening to the entire range of hydrogen concentration, which limits the relative reduction of the initial yield stress $\sigma_0(c)$ during the loading process compared to that at the beginning of loading. Therefore, application of a bilinear hydrogen softening law with mild softening up to a hydrogen concentration close to c_L^0 and a sharper softening afterwards will probably improve the simulation. As a matter of fact, the bilinear hydrogen softening effect is supported by the experimental results reported by Zhang et al. [52]. In their experiments,

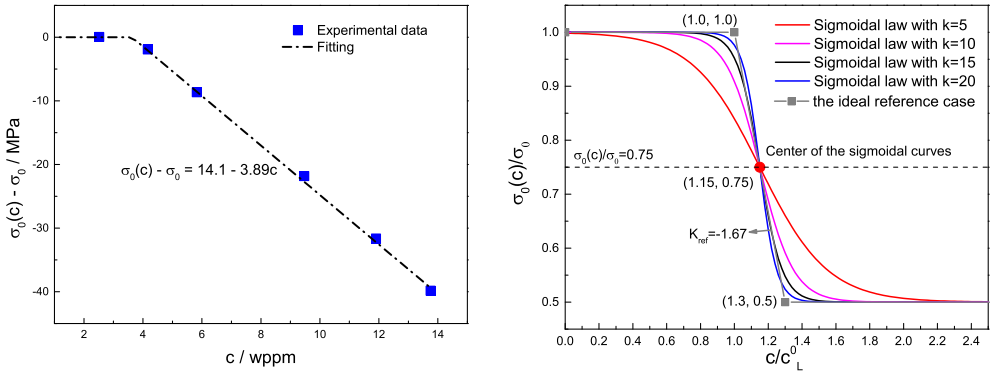

Fig. 4 (*a*) The experimentally observed hydrogen softening relation, reproduced from Zhang et al. [52]; (*b*) illustration of the sigmoidal hydrogen softening law used in this work, with a lower limit value $\zeta = 0.5$, a position parameter $x_0 = 1.15$ and different steepness parameters. The ideal reference case in (b) is a special bilinear softening scenario where no softening is observed until the transition point and linear softening observed after that point; the slope of the linear softening stage is K_{ref}.

tensile tests were performed on hydrogen charged specimens, and the yield stress was found to decrease with increasing hydrogen concentration. The relation between hydrogen induced yield stress reduction and the hydrogen concentration is reproduced in Fig. 4(a). As shown in this figure and mentioned by those authors, the hydrogen induced reduction is too small to be measured at a low hydrogen concentration, e.g. $c_0 = 2.52$ wppm, and is linearly proportional to the hydrogen concentration at high hydrogen concentrations. Apparently, two stages of hydrogen induced softening are observed and a transitional hydrogen concentration exists. Based on these considerations, we apply a hydrogen softening law with different stages of softening in this work. While the bilinear hydrogen softening law is a straightforward choice for such purpose, it introduces two additional parameters, namely the slope of the additional stage of hydrogen softening and the transitional point between the two stages. In order to keep the parameters as few as possible, the sigmoidal function is selected to construct the new hydrogen softening law

$$\frac{\sigma_0(c)}{\sigma_0} = 1 + \frac{\zeta - 1}{1 + e^{(x - x_0)k}} \tag{13}$$

where ζ is defined in Eq.(10), k is the steepness parameter of hydrogen softening effect, x represents hydrogen concentration and x_0 is the central point of the sigmoidal function thereby de-

termining the position of the hydrogen softening curve. Note that x and x_0 could be either the absolute or the normalized hydrogen concentration. To be consistent with the linear softening law used by Ahn et al. [33] (Eq.(10)), the normalized hydrogen concentration is used in this section, i.e. $x = c/c_L^0$. Upon determination of the lower limit value ζ, this law can be fully characterized by two parameters, the position parameter x_0 and the steepness parameter k. It is therefore more convenient than the bilinear form which can only be fully determined with three parameters, the first stage slope, the second stage slope and a transition point. An illustration of the sigmoidal hydrogen softening law used in this work is presented in Fig. 4(b). Following Ahn et al. [33], we set the lower limit of the initial yield stress due to hydrogen softening effect as $0.5\sigma_0$ ($\zeta = 0.5$). Assuming an ideal reference case where the initial yield stress keeps constant until the initial hydrogen concentration and decreases linearly with further increase of hydrogen until the lower limit value is reached, we can approximately obtain the smallest slope (in absolute value) that could yield lateral void growth and hence internal necking failure at a low stress triaxiality $\eta = 0.65$ as $K_{ref} = -1.67$, as shown in Fig. 4(b). Considering that $\sigma_0(c)/\sigma_0 = 0.75$ holds at the center point of all the sigmoidal functions with $\zeta = 0.5$, the intersection of the line $\sigma_0(c)/\sigma_0 = 0.75$ and the ideal reference case is taken as the center point, which gives $x_0 = 1.15$. With the position determined, we perform case study on the steepness parameter k and find that $k \geq 15$ is needed in order for the lateral void growth and internal necking failure to be observed at $\eta = 0.65$. Therefore, two cases with $k = 15$ and $k = 20$ are selected in subsequent study. The result of hydrogen-microvoid interaction simulation with the sigmoidal softening law at a low stress triaxiality $\eta = 0.7$ is shown in Fig. 3(c). In contrast to Fig. 3(a,b), obvious lateral void growth and internal necking failure are observed at a much lower effective strain, showing clearly hydrogen enhanced internal necking failure.

It should be noted that the sigmoidal hydrogen softening law is also a phenomenological form which could still be far from reality, due to the highly limited amount of experimental evidence. However, the new form is more realistic than the linear one which is an unjustified attempt to represent the HELP mechanism at the continuum level without any experimental evidence, considering the ability of the new form to model hydrogen enhanced lateral void growth at low stress triaxiality. In a generic manner, we are suggesting that the hydrogen softening effect is not "even-

ly distributed" (as the linear form indicates) over the effective range of hydrogen concentration, instead, the softening effect is less pronounced at the beginning and becomes more severe as hydrogen concentration increases. It should also be noted that the reason we select the sigmoidal form is that it has the fewest parameters, which makes it the simplest choice other than the linear form with proved limitation. This sigmoidal law depicts a scenario where the hydrogen softening curve becomes steeper with higher hydrogen concentration, and it still accounts for the hydrogen softening effect at low hydrogen concentrations, as shown in Fig. 4.

The advantage of the sigmoidal hydrogen softening law over the linear form has been verified, based on the material $M1$ which represents a material system with a low level of hydrogen trapping effect. The reason that obvious lateral void growth can be observed at low stress triaxiality is that the new hydrogen softening law is able to cause a sufficiently high level of local softening to the matrix material in the lattice hydrogen concentration dominant scenario. Such material, however, could not be related to the JIS-SGP steel [17] which is characterized by significantly higher trap binding energy. In order to verify the numerical result with the experimental observation, material $M4$, which can be qualitatively related to the bcc steel in terms of dislocation trapping characteristics is employed both with the sigmoidal hydrogen softening law and with the linear form which has an unrealistically severe softening effect $\xi = 0.3$. Considering that the specimens were electrochemically pre-charged in Matsuo et al. [17], which results in a high value of initial diffusible hydrogen concentration of $0.38 - 1.3$ wppm, the initial lattice concentration for the unit cell simulation is selected as $c_L^0 = 0.38$ wppm which is measured in the case without pre-straining. With the same sigmoidal hydrogen softening law as in Fig. 3(c), obvious hydrogen enhanced lateral void growth is observed with material $M4$, at low stress triaxiality $\eta = 0.7$, as shown in Fig. 5; with the same linear softening law as in Fig. 3(b), no hydrogen enhanced lateral void growth can be observed up to $\varepsilon_E = 1.601$, which is practically the same as Fig. 3(b) and is therefore not repeated. Up to now, we have shown that we can simulate the hydrogen enhanced lateral void growth in the low triaxiality regime with the sigmoidal hydrogen softening law, which is directly comparable to the experimental observation [17] in a qualitative manner, and this can not possibly be achieved with the linear softening law. This is direct evidence that the sigmoidal form is more realistic than the linear form of hydrogen softening effect. Strictly speaking, the initial hydrogen concentration

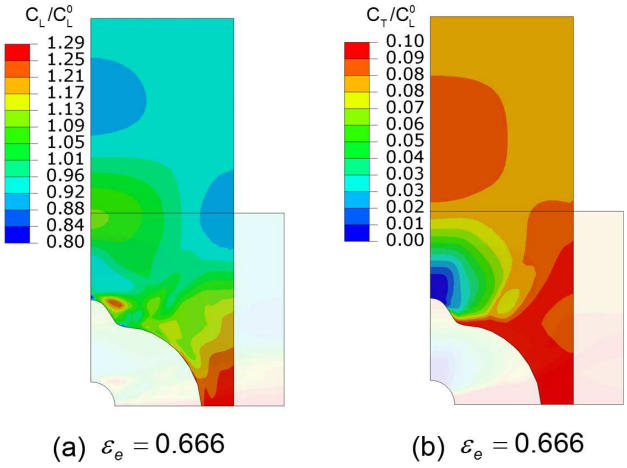

Fig. 5 Illustration of hydrogen enhanced lateral void growth for material M4 with the sigmoidal hydrogen softening law: (a) the lattice hydrogen distribution and (b) the trapped hydrogen distribution. The initial lattice hydrogen concentration after electrochemical precharging is $c_L^0 = 0.38$ wppm, and the stress triaxiality is $\eta = 0.7$. Note that void coalescence by internal necking is firstly detected at $\varepsilon_e = 0.635$.

of $c_L^0 = 0.38$ wppm used in this case is not the exact initial lattice hydrogen concentration. As reported by Matsuo et al. [17], it is the diffusible hydrogen residing in normal interstitial lattice sites and in reversible traps. According to Oriani [45], this diffusible hydrogen is in equlibrium with the strongly trapped hydrogen ($E_b = 60kJ/mol$ in the current case of bcc steel) and thus behaves as lattice hydrogen. Therefore, the initial diffusible hydrogen concentration is used in the simulation, following Ayas et al. [48]. Such practice was also adopted by Serebrinsky et al. [53] and Alvaro et al. [54] in bcc steels. In the rest part of discussion on the current case of material $M4$, the term "initial lattice hydrogen concentration" is still used in order to be consistent with the other parts of discussion on materials $M1 - M3$.

Further, we note that the level of hydrogen trapping effect in material $M4$ is actually hard to define: it has a low trap density $N_T = N_T^{exp}$ and a very high trap binding energy $E_b = 60$ kJ/mol, which seems different from material $M1$. With closer observation on the hydrogen concentration contours in Fig. 5, however, we find that these two cases are essentially the same. As discussed by Ayas et al. [48] and Jemblie et al. [46], the high energy traps (typically with $E_b > 50$ kJ/mol) will get saturated at a high initial lattice hydrogen concentration c_L^0 (in the magnitude of 0.1 wppm), after which the absolute amount of trapped hydrogen remains constant while the lattice hydrogen redistributes. Thus, the trapped hydrogen will be a small fraction of the lattice hydrogen, which

yields a lattice hydrogen dominant situation, as shown in Fig. 5. It is worth mentioning that the proportion of trapped hydrogen agrees well with that reported by Jemblie et al. [46] who used similar trapping parameters and initial hydrogen concentration. Starting from a very low initial lattice hydrogen concentration c_L^0 such as the one used in Ahn et al. [33], the trapped hydrogen will become dominant [46], and the void behavior will be different.

Therefore, the overall hydrogen trapping effect in the case with high binding energy traps such as $M4$ is determined not only by the trap density and the trap binding energy, but also by the initial condition, which is more complicated than that in the cases with low energy traps such as $M1 - M3$ where the proportion of trapped hydrogen in the total concentration does not vary with different initial conditions [46]. For parametric study about the effect of hydrogen trapping on the mechanical behavior, it is preferable to neglect the complexity brought by the high energy traps, since it is the overall hydrogen trapping effect that influences the mechanical behavior at the continuum level. Based on these considerations, only materials M1-M3 are concerned subsequently in the parametric study, and the lattice hydrogen dominant situation yielded by $M1$ is still referred to as "the low level of hydrogen trapping effect" and the other two as the medium and high levels of hydrogen trapping effect, respectively. The sigmoidal hydrogen softening law is employed in subsequent calculations, and the effect of the steepness parameter k on the failure behavior is also discussed.

2.3. Internal shearing failure criterion

When the sigmoidal law with $k = 15$ is implemented together with material $M1$ which has a low level of hydrogen trapping effect, hydrogen enhanced internal necking failure is observed over the entire range of stress triaxiality $\eta \in (0.65, 3.0)$, however, the situation is different when a different material with a high level of hydrogen trapping effect, for instance, $M3$, is considered. As shown in Fig. 6, a shear band exists in such situation, which is not observed for material $M1$. The shear band appears firstly at the void surface at the early stage of loading and propagates towards the cell boundary. This phenomenon can be rationalized with the hydrogen redistribution process. The contours of lattice and trapped hydrogen corresponding to the moment in Fig. 6(b) are plotted in Fig. 7. The trapped hydrogen distribution conforms to the plastic strain field (Fig. 7(b)), and

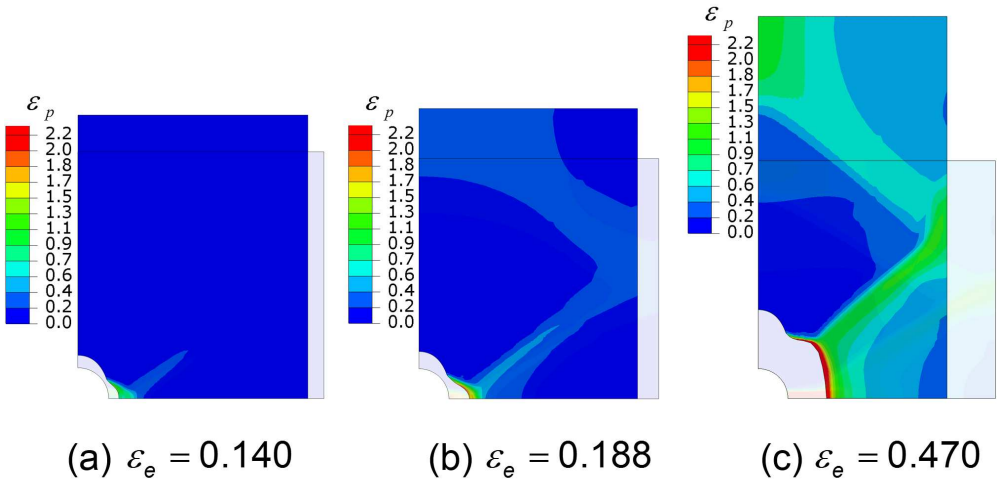

Fig. 6 The development of equivalent plastic strain inside the 2D axisymmetric unit cell with material $M3$ and the sigmoidal softening law with $k = 15$, at stress triaxiality $\eta = 0.7$: (a) at the effective strain $\varepsilon_e = 0.140$, a shear band emanates from the void surface and propagates towards the cell boundary; (b) at $\varepsilon_e = 0.188$, the shear band reaches the cell boundary for the first time; and (c) at $\varepsilon_e = 0.470$ the shear band grows to a very large extent due to the lack of material separation.

the amount is comparable to the lattice concentration, therefore, the shear band activity is strong enough to stretch the void growth from the horizontal direction to the orientation $40° - 50°$ with respect to the horizontal axis, which modifies the hydrostatic stress field, thereby moving the peak site of the lattice hydrogen concentration away from the central ligament (Fig. 7(a)). In this way, the peak site of the total hydrogen concentration is shifted from the central ligament to the newly formed shear band region, which in turn promotes further shear band development in the same direction. Similar observations were found in Ahn et al. [33]. A much higher proportion of trapped hydrogen was observed in that work due to the much smaller initial lattice concentration c_L^0 value, however, the rationalization of the shear band development is qualitatively the same as presented here. While the development of hydrogen induced shear band has been observed and phenomenologically discussed, the actual effect of the shear band on the failure of microvoid has not been treated properly, and such failure mode is even more difficult to quantify due to the lack of a proper failure criterion.

While the equivalent plastic strain could be used to illustrate the shear band development, it is not an ideal indicator for the failure onset point. As observed in Fig. 6, the equivalent plastic strain keeps increasing during the entire loading process, since no material separation in the matrix

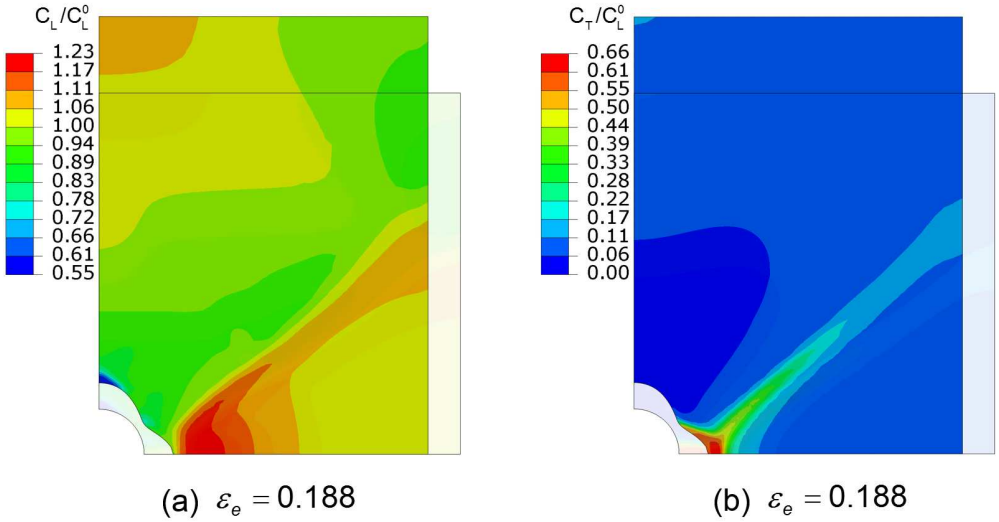

Fig. 7 Distribution of (a) the normalized lattice hydrogen concentration c_L/c_L^0 and (b) the normalized trapped hydrogen concentration c_T/c_L^0, for material $M3$ with the sigmoidal hydrogen softening law with $k = 15$, at stress triaxiality $\eta = 0.7$. The moment for these contours corresponds to that in Fig. 6(b), i.e. the shear band reaches the cell boundary for the first time; the initial lattice hydrogen concentration is $c_L^0 = 1.0$ wppm.

material is defined during the unit cell simulation. To use the equivalent plastic strain as the failure indicator, therefore, a critical value has to be selected, which is apparently a crude approximation and is highly material dependent.

A physically sound way of determining the shear induced failure is to link the failure onset point to the deformation localization into a shear band which is regarded as the result of an instability in the constitutive description of homogeneous deformation [27]. The material instability arises from loss of uniqueness of the local elastoplastic response, and according to Li and Wierzbicki [42], two classes of criteria exist: one is bifurcation analysis of strain localization such as Rudnicki and Rice [27]; the other is loss of positiveness of the second order work of the continuum, which is the sufficient condition for the loss of uniqueness of the local response [55]. Sofronis et al. [7], Liang et al. [26] studied hydrogen induced shear localization in a plane strain tensile specimen with the former approach, and Li and Wierzbicki [42] adopted the latter approach to detect failure initiation in plane strain AHSS sheets. While the effectiveness of both approaches has been verified, it is noted that they are limited to plane strain geometry and are not readily applicable to the detection of shear localization in unit cell analyses, especially the 3D situation which is involved in the current work.

To find a criterion with a wide range of applicability, we start from the very basic assumptions for the shear band localization on which the bifurcation analysis was based. According to Rudnicki and Rice [27], the deformation and stress fields are continuous from inside to outside the band at the incipient of the shear band, while the rate of deformation field becomes discontinuous with the values varying abruptly inside the band and remaining uniform outside it. This is equivalent with the statement in Needleman and Tvergaard [38] that localization of plastic flow is detected at a state where an increase in deformation occurs inside the band with no increase in deformation outside the band, i.e. $\left\|\dot{\boldsymbol{F}}^{\boldsymbol{b}}/\dot{\boldsymbol{F}}^{\boldsymbol{o}}\right\| \rightarrow \infty$, with $\dot{\boldsymbol{F}}^{\boldsymbol{b}}$ representing the rate of deformation gradient tensor inside the shear band and $\dot{\boldsymbol{F}}^{\boldsymbol{o}}$ the rate of deformation gradient tensor outside the shear band. Such criterion has been widely applied in the failure detection of a 3D unit cell in a shear field [39, 37]. As mentioned in the introduction, the width of the shear band is larger than the size of the unit cell in those studies; therefore, $\boldsymbol{F}^{\boldsymbol{b}}$ was calculated based on the boundary displacements of the entire cell and $\boldsymbol{F}^{\boldsymbol{o}}$ was approximated as the volume average of the deformation gradient of the upper part of the unit cell.

In the present study, the shear band is much smaller in width than the unit cell, and it is therefore possible to locate the shear band region and the homogeneous deformation field directly during the simulation. Considering that the norm of the rate of deformation gradient tensor $\left\|\dot{\boldsymbol{F}}\right\|$ can be regarded proportional to the plastic strain rate $\dot{\varepsilon}_p$, the criterion $\left\|\dot{\boldsymbol{F}}^{\boldsymbol{b}}/\dot{\boldsymbol{F}}^{\boldsymbol{o}}\right\| \rightarrow \infty$ could be determined in a straightforward way by observing the variation of $\dot{\varepsilon}_p^b/\dot{\varepsilon}_p^o$, with $\dot{\varepsilon}_p^b$ and $\dot{\varepsilon}_p^o$ representing the plastic strain rate in the shear band and in the homogeneous deformation field, respectively. The development of $\dot{\varepsilon}_p$ during the unit cell analysis is illustrated in Fig. 8. In Fig. 8 (a), a shear band with an abrupt increase of the plastic strain rate inside emanates from the void surface and gradually propagates towards the cell boundary; in Fig. 8 (b), the void surface and the cell boundary is linked by a fully developed shear band which is termed the “complete”shear band hereinafter. It is noted that these two figures are similar with the equivalent plastic strain contours shown in Fig. 6 (a,b). Fig. 8 (c), however, is quite different from Fig. 6 (c) in that the band in terms of plastic strain rate vanishes rather than increases with further loading. Such observation is consistent with the aforementioned criterion that an obvious discontinuity $\left\|\dot{\boldsymbol{F}}^{\boldsymbol{b}}/\dot{\boldsymbol{F}}^{\boldsymbol{o}}\right\| \rightarrow \infty$ is observed at the initiation of shear instability which finally leads to the formation of a shear band.

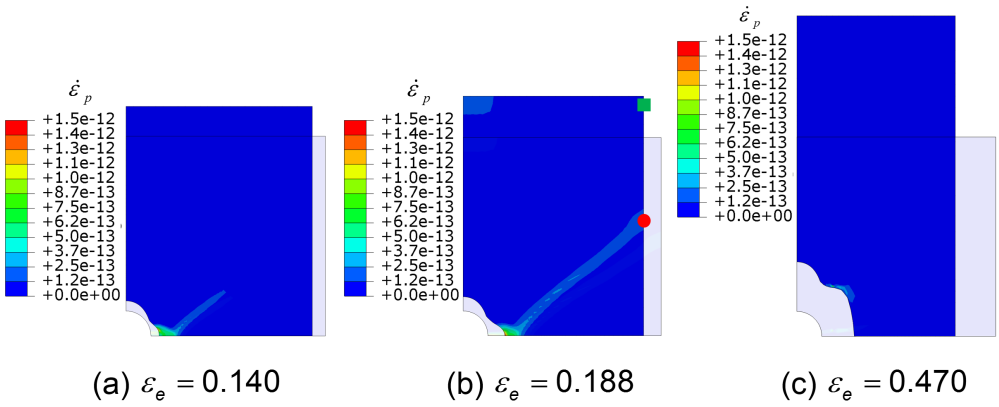

Fig. 8 The development of equivalent plastic strain rate inside the 2D axisymmetric unit cell with material $M3$ and the sigmoidal softening law with $k = 15$, at stress triaxiality $\eta = 0.7$: (a) at the effective strain $\varepsilon_e = 0.140$, a shear band with an abrupt increase of the plastic strain rate inside emanates from the void surface and gradually propagates towards the cell boundary; (b) at $\varepsilon_e = 0.188$, the shear band reaches the cell boundary for the first time; and (c) at $\varepsilon_e = 0.470$, the difference of the plastic strain rate inside and outside the shear band vanishes.

The discontinuity disappears in the post-initiation regime where no instability is expected.

Therefore, the occurrence of discontinuity between the rate of deformation gradients in the shear band and in the homogeneous deformation field, or equivalently $\dot{\varepsilon}_p^b/\dot{\varepsilon}_p^o \to \infty$, is a unique event that can be adopted as the (shear) localization indicator. In the unit cell analyses, it is reasonable to define failure initiation as the point where a "complete"shear band linking the void surface and the cell boundary is detected. Considering that the shear band initiates from the void surface, the intersection of the anticipated shear band and the cell boundary should be taken as the critical site for formation of the "complete"shear band. Based on this consideration, the plastic strain rate history at this site (circular point in Fig. 8 (b)) and that at a point (rectangular point in Fig. 8 (b)) inside the homogeneous deformation field are recorded and plotted in Fig. 9(a). The trend in the development of the plastic strain rate $\dot{\varepsilon}_p$ observed in this figure is consistent with that in Fig. 8. At the initial stage of loading where the shear band has not reached the cell boundary, both points lie in the homogeneous deformation field and practically no difference in $\dot{\varepsilon}_p$ exists. Around the effective strain $\varepsilon_e \approx 0.188$, a sudden increase of $\dot{\varepsilon}_p$ at the circular point inside the anticipated shear band occurs indicating that a "complete"shear band is formed and failure is triggered. As loading further increases, post-initiation condition dominates and the difference in $\dot{\varepsilon}_p$ vanishes.

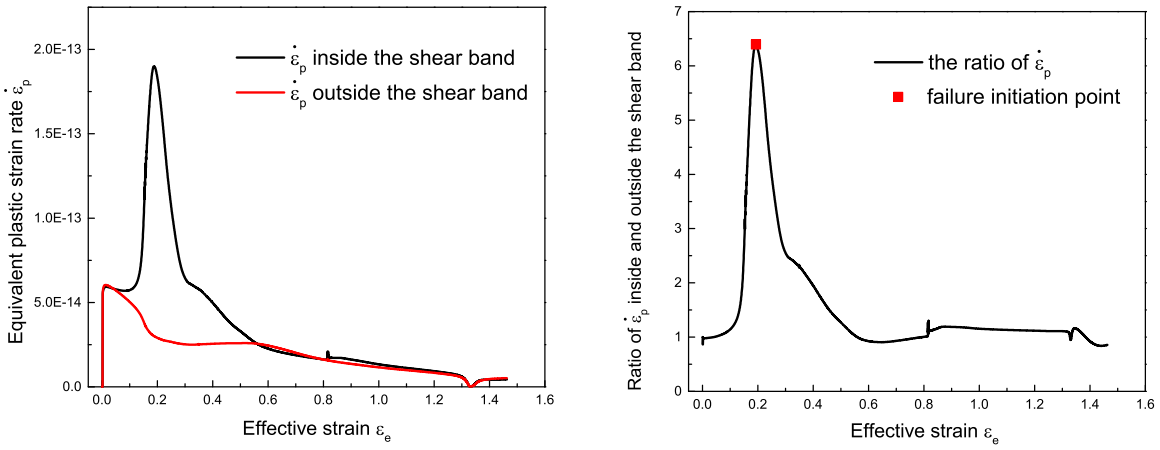

Fig. 9 (*a*) The histories of the equivalent plastic strain rate $\dot{\varepsilon}_p$ inside and outside the shear band; (*b*) Ratio of $\dot{\varepsilon}_p$ inside and outside the shear band. The material is $M3$ and the stress triaxiality is $\eta = 0.7$.

To illustrate the procedure more clearly, the ratio between $\dot{\varepsilon}_p$ at the critical site and that in the homogeneous deformation field is plotted in Fig. 9(b), and the peak point of this curve, which is a unique event, is selected as the failure initiation point of the unit cell due to shear localization.

As shown in Fig. 6(b), a branch of shear band is observed, linking the symmetry axis and the intersection point on the cell surface. Similar scenario is also indicated in Fig. 8(b), but the branch there is overshadowed due to the wide range of contour legend. If we narrow the range of contour legend down for the same figure, this branch of shear band in terms of plastic strain rate will become visible, as shown in Fig. 10(b). This is caused by the boundary conditions applied to the unit cell. As presented in section 2, the unit cell analysis is performed with no external shearing components, meaning that the cell surfaces are kept flat, that is, there is no "free surface" during the simulation. As a consequence, when the shear band reaches the cell surface, phenomenologically, it has to "bounce back" towards the symmetry axis. In fact, Fig. 10(b) depicts two identical shear bands originating from the void surfaces in neighboring unit cells and crossing each other at the intersection point that looks like "reflection". In this sense, the intersection point of the "complete" shear band and the cell surface, which is selected as the failure initiation site, is actually the first crossing point of the two identical shear bands originating from adjacent void surfaces. Considering that the "reflection" occurs almost the same time as the formation of

the "complete" shear band, the failure criterion presented above is sufficiently accurate. Similar phenomena of shear band "reflection" are observed in the 3D scenario, e.g. Fig. 18, and the same principle applies.

The effectiveness of the new failure criterion, i.e. $\dot{\varepsilon}_p^b/\dot{\varepsilon}_p^o \to \infty$, is verified in Appendix A. This criterion is applied to determination of the hydrogen induced internal shearing failure point throughout the subsequent study and is referred to as the internal shearing failure criterion hereinafter. The mesh sensitivity of the internal shearing failure criterion is discussed in Appendix B.

3. Hydrogen-microvoid interactions

Up to now, the framework for hydrogen-microvoid interaction simulation is complete. Before going to the results, a short recap of the numerical procedure is presented. Two different sigmoidal hydrogen softening laws with $k = 15$ and $k = 20$ are considered, representing a medium and a large steepness of the softening effect, respectively. It should be noted that the softening law illustrated in Fig. 4(b) was plotted versus the normalized hydrogen concentration, and the purpose was to be consistent with that in Ahn et al. [33] when it was compared to the linear softening law. In reality, the sigmoidal hydrogen softening law should be viewed as a function of the absolute value of hydrogen concentration c, which can be directly obtained from Eq.(13)

$$\frac{\sigma_0(c)}{\sigma_0} = 1 + \frac{\zeta - 1}{1 + e^{(c-1.15c_L^0)\cdot k/c_L^0}} \tag{14}$$

and the term c_L^0 should be regarded only as a parameter related to the position of the sigmoidal curve rather than the initial lattice hydrogen concentration. In subsequent study, the parameter c_L^0 is set as $c_L^0 = 1.0$ wppm. The initial hydrogen concentration after pre-charging is now denoted c_0, and it can be various values. We choose $c_0 = c_L^0$ in subsequent simulations on materials $M1 - M3$, which gives an initial hydrogen concentration of similar magnitude as that measured after electrochemical pre-charging in steels. Note that the value of c_L^0 is actually not important during subsequent study, since the materials $M1 - M3$ to be concerned later are characterized by a low trap binding energy, meaning that the proportion of trapped hydrogen, and therefore

the mechanical behavior of the unit cell, is independent of c_L^0, as discussed in subsection 2.2. The lower limit for the softening effect is kept as $\zeta = 0.5$. As mentioned in subsection 2.2, the sigmoidal hydrogen softening law depicts a scenario where hydrogen exerts a mild softening effect below a certain hydrogen concentration ("turning point") and a severe softening effect beyond that, which is different from the linear softening law representing an "evenly distributed" softening effect. This indicates that the results of hydrogen-microvoid interaction will inevitably be dependent on the relation between the initial hydrogen concentration and the "turning point", which makes the situation more complicated. However, this is the natural consequence of introducing the more realistic hydrogen softening effect which is not "evenly distributed", and it will not affect the outcome of this study, since no variation in the initial hydrogen concentration is concerned here. Throughout this work, the initial hydrogen concentration is fixed at a value close to the "turning point", which yields the strongest hydrogen effect on the microvoid behavior.

The three materials $M1$, $M2$ and $M3$, shown in Table 1, are selected, representing low, medium and high levels of hydrogen trapping effect. The failure point of unit cell is determined as the occurrence of internal necking or internal shearing. Both the $2D$ axisymmetric and the 3D unit cell analyses are performed, revealing a thorough picture of the hydrogen failure loci.

3.1. Failure loci in 2D stress space

There exists two mutually exclusive modes of failure during hydrogen-microvoid interaction, namely the hydrogen enhanced internal necking failure and the hydrogen induced internal shearing failure. Under the same hydrogen softening law with $k = 15$, the former mode is observed in material $M1$ and the latter is observed in materials $M2$ and $M3$. The common feature is that both failure modes are associated with the event of deformation localization. Another phenomenon that could be associated with deformation localization is the post-shear necking point which is an artificial result due to the lack of material separation after shear localization in the matrix material, as discussed in the previous section. According to the discussion on deformation localization earlier, these three events should be accompanied by a discontinuity in the rate of deformation field, i.e. existence of a region inside which there is an abrupt increase of the plastic strain rate $\dot{\varepsilon}_p$. To verify this point and to investigate the features of these events, the contours of $\dot{\varepsilon}_p$ corresponding

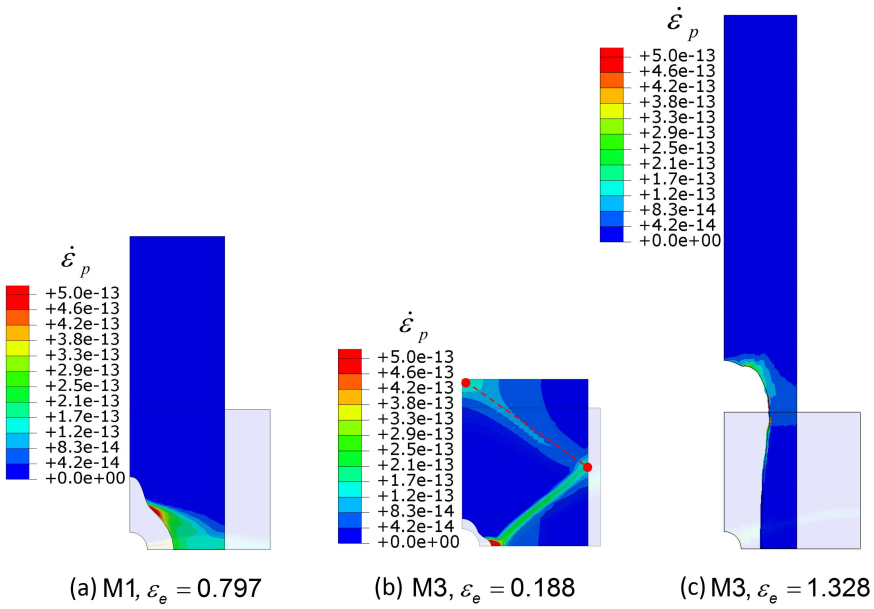

Fig. 10 Contours of $\dot{\varepsilon}_p$ for: (a) internal necking failure point with material $M1$, (b) internal shearing failure point with material $M3$ and (c) post-shear necking point with material $M3$. The stress triaxiality is $\eta = 0.7$. Note that figure (b) is the same one as Fig. 8(b), and the different contour color is due to the difference in the legends. The dashed line represents the shear band "reflection".

to the occurrence of the localization events are shown in Fig. 10. The stress triaxiality is $\eta = 0.7$; the internal necking related events are detected with the void coalescence criterion in Koplik and Needleman [31] and the shear localization event with the internal shearing failure criterion. Clearly, a sudden increase of $\dot{\varepsilon}_p$ is observed in all these contours, which marks the region where strain localization happens. In Fig. 10(a), strain localization happens at the central ligament between two adjacent voids causing hydrogen enhanced internal necking failure in material $M1$. In Fig. 10(b), deformation localizes inside a shear band causing hydrogen induced internal shearing failure in material $M3$. With further loading, the cell continues deforming beyond the internal shearing failure point in Fig. 10(b) and the void is stretched in the direction coinciding with the shear band orientation; at a large effective strain value $\varepsilon_e = 1.328$, the void coalescence condition proposed by Koplik and Needleman [31] is met and strain localization in a manner of necking, i.e. the post-shear necking point, is observed. It is noted that necking occurs close to the void surface from which the shear band emanates in Fig. 10(c), rather than in the central ligament between two voids in Fig. 10(a), that is, the shear band stretches the void along the diagonal direction thereby moving

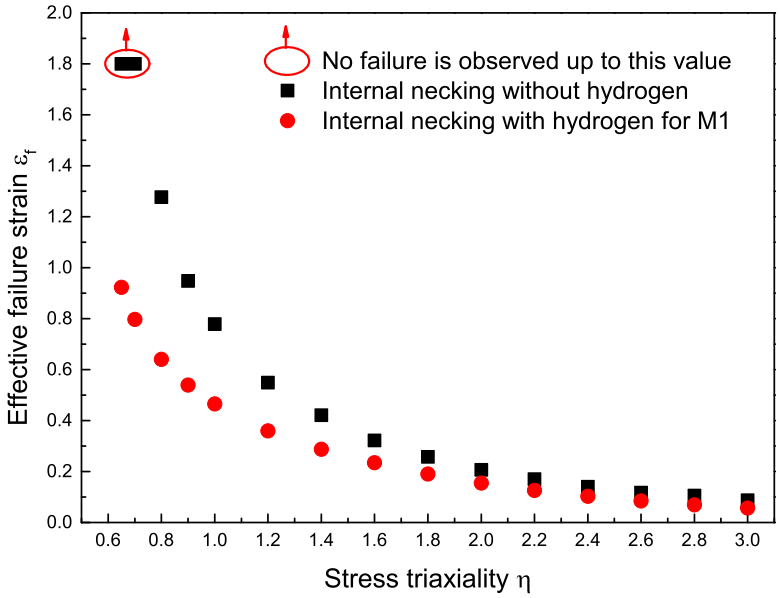

Fig. 11 Comparison between the failure locus without hydrogen and that with hydrogen for material $M1$ with a low level of hydrogen trapping effect.

the necking site away from the central ligament which is the most favorable site for internal necking. Therefore, the post-shear necking strain ($\varepsilon_e = 1.328$) in material $M3$ is significantly larger than the internal necking failure strain ($\varepsilon_e = 0.797$) in material $M1$, although the same hydrogen softening law is applied. Further, it can be shown that the effect of the shear band in moving the necking site away from the central ligament becomes weaker as stress triaxiality increases, i.e. the post-shear necking site is closer and closer to the central ligament, and the difference between the internal necking failure strain and the post-shear necking strain becomes less pronounced at larger stress triaxiality, for instance, $\eta = 1.0$, but this discussion is not extended due to the artificial nature of the post-shear necking point. Subsequently, the loci related to these three deformation localization related events are presented and discussed. If not mentioned, the steepness parameter of the sigmoidal hydrogen softening law is $k = 15$.

In the absence of hydrogen, failure occurs by internal necking, and the failure locus without hydrogen is obtained and plotted in Fig. 11 together with that in the presence of hydrogen for material $M1$. In the presence of hydrogen with a low level of trapping effect, internal necking failure is observed over the entire range of stress triaxiality concerned. The internal necking failure strains

with hydrogen are smaller than those without hydrogen, showing that hydrogen induced softening effect promotes internal necking failure at all the stress states concerned. Moreover, hydrogen enhanced internal necking failure effect is quite significant in the low stress triaxiality regime, for instance, no failure was observed up to a large effective strain $\varepsilon_e = 1.8$ at $\eta = 0.7$ in the absence of hydrogen while the introduction of hydrogen lowers the failure strain to $\varepsilon_f = 0.797$, which corresponds to over 50% reduction in ductility. The effect is less pronounced in the high stress triaxiality regime, while a 28% reduction in ductility is still observed at $\eta = 3.0$. It is therefore concluded that hydrogen could reduce the ductility of the material through the HELP mechanism. Meanwhile, it is noted that the reduction in ductility is achieved by hydrogen enhanced lateral void growth and coalescence, therefore, large dimples will still be observed at failure.

Investigation on material $M3$ reveals a different picture regarding the dimple size at failure. The failure loci without hydrogen and with hydrogen for material $M3$ are illustrated in Fig. 12. The loci related to the internal shearing failure and the post-shear necking point observed in this material are both presented. Interestingly, a transition of failure mode is observed. In the range of $\eta \in (0.65, 1.8)$, a clear formation of shear band is observed in the presence of hydrogen, which indicates failure of the unit cell by internal shearing. The post-shear necking points in this range are linked via a dashed curve, implying that they are artificial products due to the lack of material separation after shear localization and cannot be achieved in reality. In contrast, the triangular dots representing the realistic internal shearing failure points are linked via a solid line. In the high triaxiality regime, however, no shear band is observed in the loading process and failure occurs by internal necking. Specifically, the shear band is not so pronounced but still recognizable at $\eta = 1.8$, but it becomes negligible at $\eta = 2.0$ and completely disappears afterwards. Therefore, we can term the position $\eta = 2.0$ as the conversion point from the internal shearing failure mode to the internal necking failure mode, which is marked in Fig. 12. Beyond this point, internal necking failure points are detected as linked via the solid line. Note that these points represent realistic failure events since they are not preceded by the shear band formation. In summary, the real failure locus with hydrogen for material $M3$ consists of two branches, the internal shearing failure branch and the internal necking failure branch. These branches are divided by the failure mode conversion point which in the present case is found at $\eta = 2.0$. Further observation on Fig. 12 reveals that

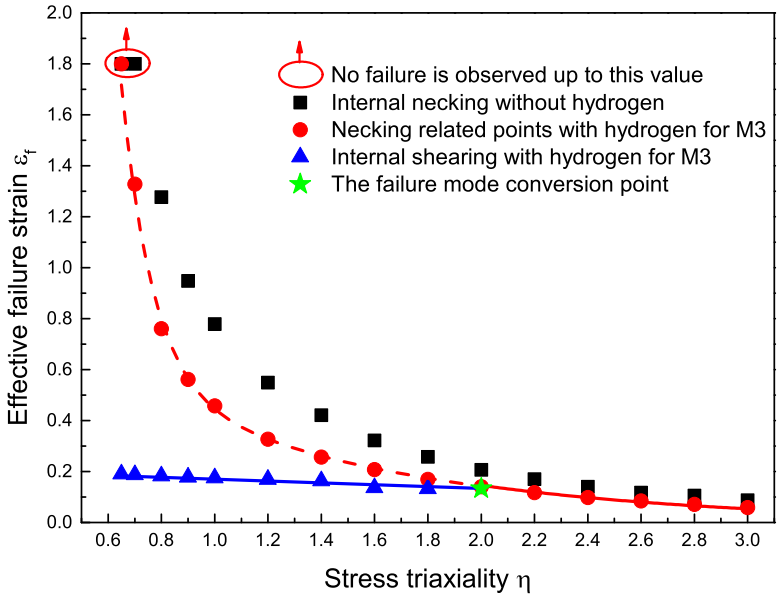

Fig. 12 Comparison between the failure locus without hydrogen and that with hydrogen for material $M3$ with a high level of hydrogen trapping effect.

the stress triaxiality dependence of the failure locus on the internal shearing failure branch is practically eliminated, compared to that without hydrogen. The stress triaxiality dependence is maintained in the internal necking failure branch. Upon closer observation at the internal shearing failure branch in Fig. 12, we find that it seems to slightly decrease in a linear manner with stress triaxiality, which is still unpronounced compared to the case without hydrogen. Therefore, this branch could be treated either as constant or as a linearly decreasing function of stress triaxiality, which is straightforward to implement in engineering practice. With the failure locus marked by the solid lines, hydrogen enhanced premature failure is clearly illustrated. Finally, the internal shearing failure branch, together with the shear band illustration in Fig. 10(b), shows that the hydrogen induced internal shearing failure occurs at very early stage of loading with no substantial void growth, that is, the dimples remain quite small at failure and could even be indistinguishable.

The failure loci with hydrogen for materials $M1$ and $M3$ are compared in Fig. 13. It is observed that the hydrogen induced internal shearing failure strain is much smaller than the hydrogen enhanced internal necking failure strain in the low triaxiality regime for the same hydrogen soft-

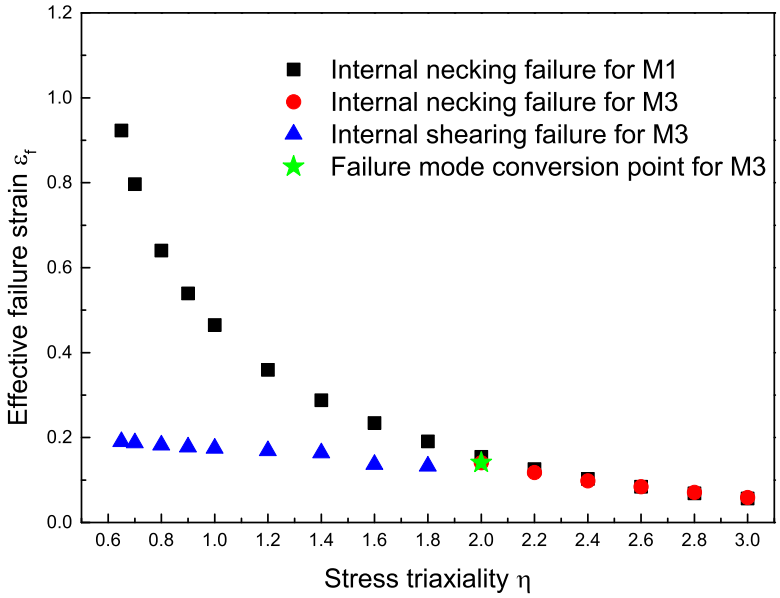

Fig. 13 Comparison between the failure locus for material $M1$ and that for material $M3$. Both are obtained in the presence of hydrogen, at the same sigmoidal hydrogen softening law with the steepness parameter $k = 15$.

ening law. It also shows that practically no difference exists between the internal necking failure loci for materials $M1$ and $M3$ beyond the failure mode conversion point, indicating that the effect of trapped hydrogen on hydrogen enhanced internal necking failure in the high stress triaxiality regime is limited. The reason is that trapped hydrogen concentrates at the void surface instead of inside the cell matrix at high stress triaxiality, it therefore softens the edge material locally and contributes only a small part to the internal necking failure mode.

The discussion so far has been based on the same sigmoidal hydrogen softening law with $k = 15$, and only the low and high levels of hydrogen trapping effects have been concerned. The failure loci with a large steepness parameter k and a medium level of hydrogen trapping effect are presented and discussed subsequently. The case with material $M2$ in combination with $k = 15$ and that with material $M3$ in combination with $k = 20$ are concerned, and both are compared to the case with material $M3$ and $k = 15$ discussed earlier.

The comparison between the failure loci with the medium ($M2$) and high ($M3$) levels of hydrogen trapping effect is given in Fig. 14. The trend of the failure locus for material $M2$ is analogous

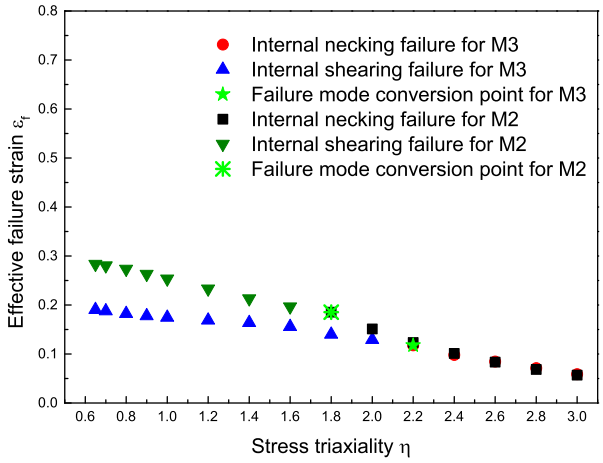

Fig. 14 Comparison between the failure locus for material $M2$ and that for material $M3$. Both are obtained in the presence of hydrogen, at the same sigmoidal hydrogen softening law with the steepness parameter $k = 15$.

to that for material $M3$ in that the internal shearing failure branch and the internal necking failure branch are observed in both cases. For material $M2$, an overall increase in the effective failure strain values related to the internal shearing failure branch is observed, while the stress triaxiality dependence of this branch remains still unpronounced, compared to the triaxiality dependence in the absence of hydrogen as shown in Fig. 12. Meanwhile, the conversion point marking the transition of failure mode from internal shearing to internal necking is moved forward in the case with material $M2$, from $\eta = 2.0$ to $\eta = 1.8$. Such observations indicate more intensive shear band activity in the hydrogen-microvoid interaction at a higher level of hydrogen trapping effect. On the internal necking failure branches, the difference in the effective failure strain values for material $M3$ and for material $M2$ is still minor, further supporting the conclusion that the effect of trapped hydrogen on hydrogen enhanced internal necking failure in the high stress triaxiality regime is limited.

The influence of hydrogen softening is investigated by comparing the failure loci at sigmoidal softening laws with different steepness parameters k, as shown in Fig. 15. Both loci are obtained for the same material $M3$, with $k = 15$ and $k = 20$ representing a medium and a large steepness of hydrogen softening effect, respectively. The failure loci at $k = 20$ is analogous to that at $k = 15$ in that the internal shearing failure branch and the internal necking failure branch are observed

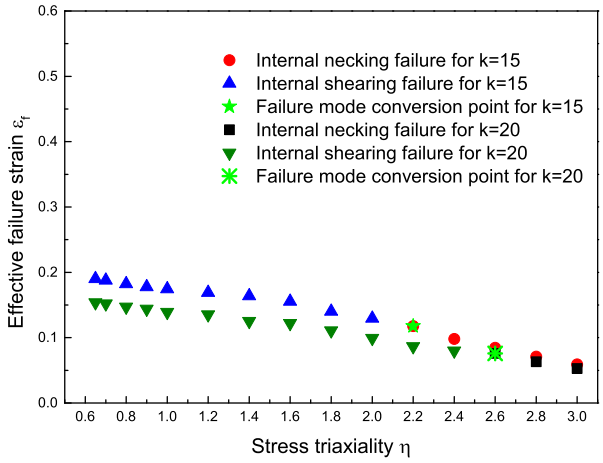

Fig. 15 Comparison between the failure locus at a sigmoidal hydrogen softening law with $k = 15$ and that at a sigmoidal hydrogen softening law with $k = 20$. Both are obtained in the presence of hydrogen, for the same high level of hydrogen trapping effect (material $M3$).

in both cases. The internal shearing failure branch at $k = 20$ is obviously lower than that at $k = 15$ while the stress triaxiality dependence remains unpronounced, compared to the triaxiality dependence in the absence of hydrogen as shown in Fig. 12. The failure mode conversion point is postponed from $\eta = 2.0$ to $\eta = 2.6$, indicating that the shear band activity is enhanced due to the larger steepness of hydrogen softening effect. The difference in the effective failure strain values on the internal necking branches in the high stress triaxiality regime in Fig. 15 is larger than that in Fig. 13 or Fig. 14, which is not distinguishable but can be verified by directly comparing the failure strain values at these points. Therefore, the variation of hydrogen softening effect has more pronounced influence on the internal necking failure branches compared with the variation of hydrogen trapping effect, since it directly influences the level of local softening, regardless of which hydrogen population is dominant in the internal necking failure process.

Finally, the initial void volume fraction f_0 as a potential factor is discussed. The investigation so far is based on a relatively large initial void volume fraction $f_0 = 0.001$. However, f_0 can be smaller in reality, and it is therefore important to verify the transferability of the current conclusions to a smaller f_0. For such purpose, $f_0 = 0.0001$ is selected and coupled hydrogen diffusion-unit cell analyses are performed for material $M3$ at the sigmoidal hydrogen softening law with $k = 15$. The hydrogen failure locus for $f_0 = 0.0001$ is constructed and compared with that for $f_0 = 0.001$,

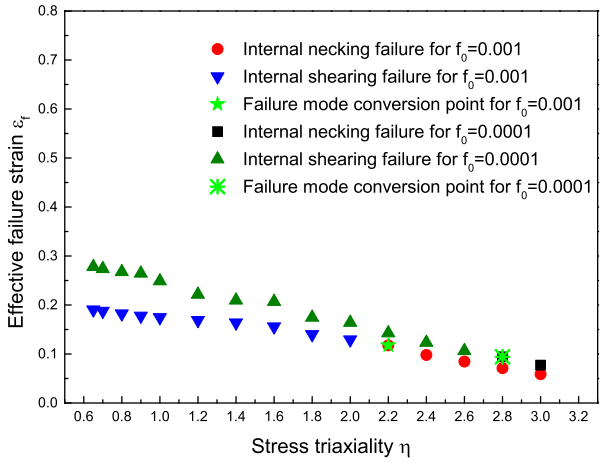

Fig. 16 Comparison between the failure locus for the initial void volume fraction $f_0 = 0.001$ and that for the initial void volume fraction $f_0 = 0.0001$. Both are obtained in the presence of hydrogen, for the same high level of hydrogen trapping effect (material $M3$) and at the sigmoidal hydrogen softening law with $k = 15$.

as shown in Fig. 16. Similar with the previous observations, the hydrogen failure locus consists of the internal shearing failure branch and the internal necking failure branch in the case with a smaller initial void volume fraction. The internal necking failure strain values for $f_0 = 0.0001$ are larger than those for $f_0 = 0.001$ due to the smaller initial void volume fraction, which is consistent with the observations reported by Kim et al. [56] in the absence of hydrogen. The internal shearing failure branch for $f_0 = 0.0001$ is generally higher than that for $f_0 = 0.001$, which is reasonable. The failure mode conversion point is significantly postponed for $f_0 = 0.0001$, suggesting that the smaller initial void volume fraction favors internal shearing failure mode in the high stress triaxiality regime. Despite the difference in exact values, it is noted that similar trend as for $f_0 = 0.001$ is observed for $f_0 = 0.0001$, indicating that the conclusions obtained for $f_0 = 0.001$ are generally transferrable to cases with smaller initial void volume fractions. Therefore, only the case with $f_0 = 0.001$ is discussed in subsequent study.

At the end of this part, it needs to be mentioned that the trends revealed about the hydrogen enhanced internal necking failure and the hydrogen induced internal shearing failure should be viewed as generic conclusions applicable to a variety of materials instead of special products under certain combination of parameters. With different materials and hydrogen softening laws, the conclusions are not qualitatively changed. For instance, for material $M4$ and an initial lattice

hydrogen concentration $c_L^0 = 0.38$ wppm, which yields a lattice hydrogen dominant situation, as shown in Fig. 5, hydrogen enhanced internal necking failure is observed for all the stress triaxiality with the sigmoidal hydrogen softening law, and the hydrogen failure locus is therefore very similar to that in Fig. 11, which is not repeated here. The same material $M4$ was used by Ahn et al. [33], however, very small initial lattice hydrogen concentration c_L^0 was applied there, yielding a trapped hydrogen dominant situation due to the reasons elaborated in subsection 2.2. Therefore, hydrogen induced internal shearing failure mode was produced in that study; based on the same parameters and the linear hydrogen softening law adopted by Ahn et al. [33], we have established the hydrogen failure locus, and we find that it consists of an internal shearing branch and an internal necking branch and that the trends conform qualitatively to the conclusions presented above.

3.2. Failure loci in 3D stress space

In order to get a more detailed description of the dependence of hydrogen influenced failure loci on the stress state, the Lode parameter effect should be taken into account, which requires 3D unit cell analyses. The hydrogen-microvoid interaction results obtained via 3D unit cell analyses are presented here. The hydrogen enhanced internal necking failure is detected by the void coalescence criterion proposed by Koplik and Needleman [31] and the hydrogen induced internal shearing failure by the newly proposed internal shearing failure criterion. The discussion will mainly focus on the internal shearing failure branch observed in material $M3$ as shown in Fig. 12. The influence of the stress triaxiality η and the Lode parameter L on the internal necking failure locus with hydrogen for material $M1$ is analogous to that on the internal necking failure locus without hydrogen, which has been discussed in detail by Gao and Kim [57], Yu et al. [32] and is therefore introduced only briefly here. When material $M1$, representing a low level of hydrogen trapping effect is considered, failure occurs in the manner of internal necking over the entire 3D stress space, and the effective failure strain lowers with stress triaxiality at a constant Lode parameter, as shown in Fig. 11. When the stress triaxiality is fixed, the effective failure strain increases with the Lode parameter, and an instance at $\eta = 1.0$ is given in Fig. 17(a).

The Lode effect on the failure locus has been studied by 3D unit cell analyses in the combined tension and shear scenario [39, 37], in the absence of hydrogen. As mentioned in subsection 2.3,

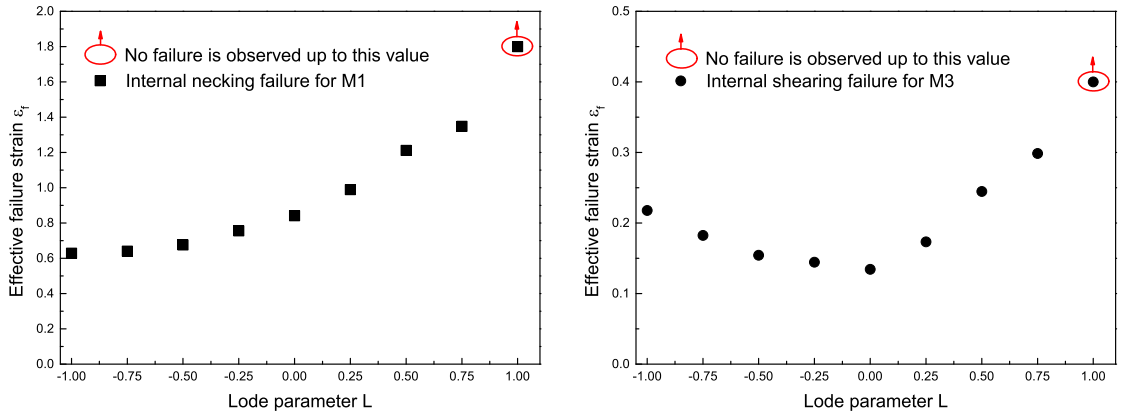

Fig. 17 (*a*) Internal necking failure locus versus the Lode parameter for material $M1$ at a constant stress triaxiality $\eta = 1.0$; (*b*) internal shearing failure locus versus the Lode parameter for material $M3$ at a constant stress triaxiality $\eta = 1.0$. Both are obtained in the presence of hydrogen, at the sigmoidal hydrogen softening law with $k = 15$.

however, the situation with our current unit cell study in the presence of hydrogen is quite different in that the shear band is much smaller in width compared to the cell size, therefore, the existing theory about the Lode effect is not directly applicable to the hydrogen induced internal shearing failure locus here. The influence of the Lode parameter on hydrogen induced internal shearing failure has not been investigated to the best of our knowledge. To study this, the stress triaxiality is fixed at $\eta = 1.0$ and the internal shearing failure locus with hydrogen for material $M3$ at the sigmoidal hydrogen softening law with $k = 15$ is constructed versus the Lode parameter, as shown in Fig. 17(b). The effect of Lode parameter here is apparently different from that in Fig. 17(a). The effective internal shearing failure strain decreases with the Lode parameter in the negative regime $L \in (-1.0, 0.0)$ while increasing in the positive regime $L \in (0.0, 1.0)$. According to Bai and Wierzbicki [58], $L = -1.0$ represents the axisymmetric tension situation, $L = 1.0$ the equiaxial tension situation and $L = 0$ the plane strain tension or the generalized shear situation, note that the Lode angle parameter instead of the Lode parameter was used in that work. Therefore, an intuitive impression on Fig. 17(b) is that the hydrogen induced shear localization is most prone to occur in a plane strain or generalized shear scenario. Specifically, the failure point corresponding to $L = -1.0$ in Fig. 17(b) could represent a notched tensile bar while the point corresponding to $L = 0$ could represent a plane strain notched tensile specimen, considering that $\eta = 1.0$. More

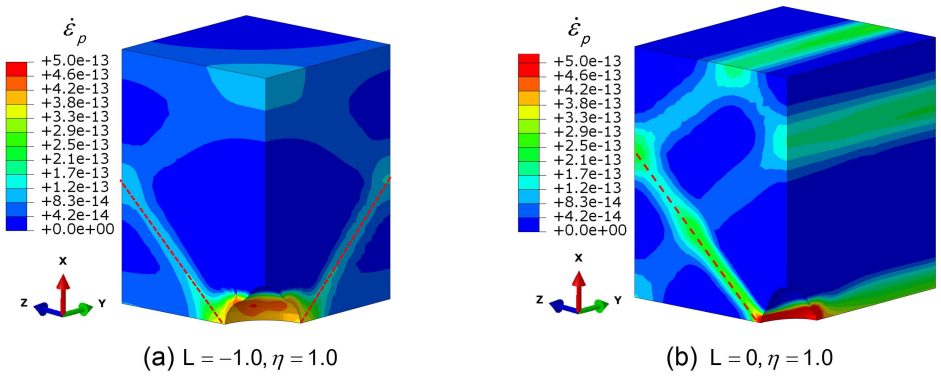

Fig. 18 Contours of the plastic strain rate at the internal shearing failure point (material $M3$) for (a) $L = -1$, $\eta = 1.0$ and (b) $L = 0$, $\eta = 1.0$. Clearly, shear localization can be observed in both figures, and the dominant shear bands are marked with dashed lines.

details regarding these two cases can be found by comparing the contours of plastic strain rate corresponding to these failure points, as shown in Fig. 18. Both cases are characterized by the existence of fully developed shear band(s) linking the void surface and the cell boundary, which signifies the initiation of internal shearing failure as discussed in subsection 2.3. It is observed that shear bands occur on both surfaces perpendicular to the Y and Z axes in Fig. 18(a), while only one apparent shear band occurs on the surface perpendicular to the Y axis in Fig. 18(b). Clearly, failure in Fig. 18(a) occurs in an axisymmetric manner, while that in Fig. 18(b) occurs in a plane strain manner with the Y axis being the thickness direction along which no variation in the contour value exists. It is further noticed that Fig. 18(b) is actually comparable to the case of plane strain tensile specimen shown in Fig. A.21(b), except that a smaller stress triaxiality was applied to that case with $\eta \approx 0.57$ [58]. No initial perturbation in the hydrogen distribution, which was necessary for triggering the shear band localization in Fig. A.21(b), is needed in the current case since the central void in the unit cell serves as a geometric imperfection which is an equivalent stimulating factor for shear band formation. Finally, the influence of stress triaxiality on the internal shearing failure locus is discussed. While the variation of the internal shearing failure loci with stress triaxiality was so small in Fig. 14 and Fig. 15 compared to the necking related loci that they could practically be taken as stress triaxiality independent in engineering failure assessment, there existed a clear trend that this branch lowers slightly with increase of stress triaxiality. Therefore, the internal shearing failure branch is picked out and discussed individually.

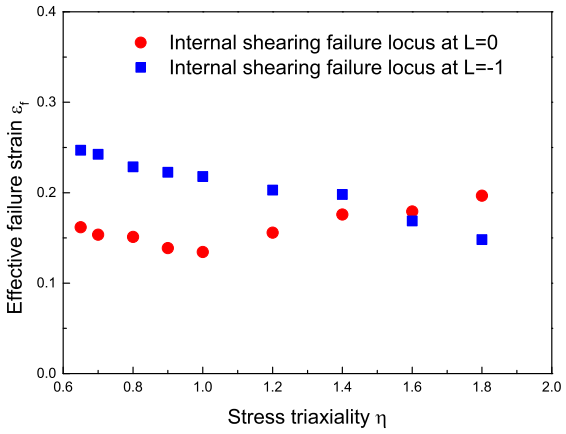

Fig. 19 Internal shearing failure loci versus stress triaxiality at constant Lode parameters $L = 0$ and $L = -1.0$. Both are obtained in the presence of hydrogen, for the same high level of hydrogen trapping effect (material $M3$) and at the sigmoidal hydrogen softening law with $k = 15$.

Two cases are considered here, with constant Lode parameters $L = -1.0$ and $L = 0$, respectively. The internal shearing failure loci are plotted against stress triaxiality in Fig. 19. The position and trend of the internal shearing failure locus for $L = -1.0$ correspond very well to the internal shearing failure branch in Fig. 12 for the same material and hydrogen softening law obtained from the 2D axisymmetric unit analyses, and the small difference in the actual values of effective failure strain is due to the fact that the shape of the cell in the current 3D situation is assumed to be cubic while that in the 2D axisymmetric situation was assumed to be cylindrical. The effective internal shearing failure strain in the axisymmetric situation $L = -1.0$ decreases consistently with increase of stress triaxiality until $\eta = 2.0$ where the internal necking failure takes place. In the case with $L = 0$, however, the effective internal shearing failure strain decreases first, then increases with stress triaxiality, with the trend inversion point being approximately $\eta = 1.0$. To account for the different trends observed in cases with $L = -1.0$ and $L = 0$, the contours of plastic strain rate corresponding to the failure points in this figure are examined. In the former case, the angle of the "complete"shear band at failure with respect to the X axis is found to be almost constant for the entire range of stress triaxiality concerned, that is, the intersection point of the shear band and the cell boundary keeps the same as shown in Fig. 18(a) from $\eta = 0.65$ to $\eta = 1.8$. In the latter, the angle keeps constant up to $\eta = 1.0$, as shown in Fig. 18(b) and Fig. 20(a), while it becomes increasingly larger with further increase of stress triaxiality, i.e. the intersection point becomes

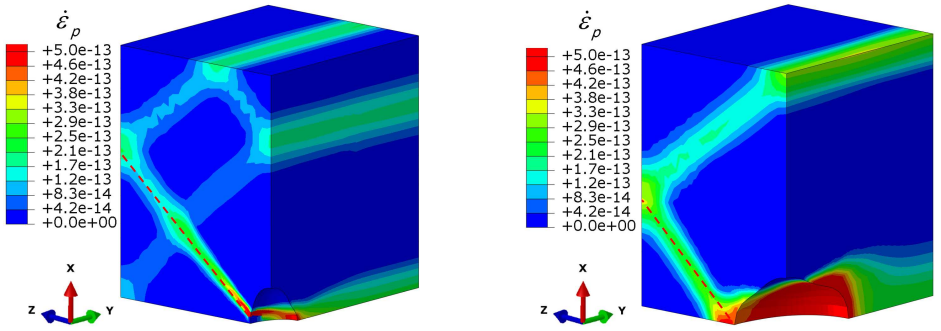

Fig. 20 Contours of the plastic strain rate at the internal shearing failure point (material $M3$) for (a) $L = 0,\ \eta = 0.7$ and (b) $L = 0,\ \eta = 1.8$. Clearly, shear localization can be observed in both figures, and the dominant shear bands are marked with dashed lines.

lower and lower; the obvious variation of this angle is illustrated in Fig. 20 by comparison between the cases of $L = 0,\ \eta = 0.7$ and $L = 0,\ \eta = 1.8$. It is further noted that the decreasing trend of the internal shearing failure locus in $L = 0$ maintains as long as the angle of shear band keeps constant (until $\eta = 1.0$), therefore, we infer that the inversion of this trend after $\eta = 1.0$ is caused by the change in the angle of the shear band, which does not occur in the axisymmetric situation.

4. Summary

Hydrogen-microvoid interactions are studied at the continuum scale via fully coupled hydrogen diffusion-unit cell analyses under the framework of HELP mechanism.

A sigmoidal hydrogen softening law is proposed to replace the linear form which assumed an "evenly distributed"hydrogen softening effect over the effective range of hydrogen concentration. The sigmoidal hydrogen softening law represents essentially a "piece-wise"hydrogen softening scenario with a mild initial degradation on the yield stress σ_0 followed by a rapid one, and it is therefore able to yield a high level of softening effect for certain values of initial hydrogen concentration. It enables us to reproduce the experimental observation [17] of hydrogen enhanced lateral void growth at low stress triaxiality, which is not possible using the linear form.

The hydrogen induced failure is found to be dependent on the level of hydrogen trapping effect as well as on the stress triaxiality. In the low stress triaxiality regime and for a low level of hydrogen trapping effect, hydrogen enhanced internal necking failure is observed; when the level of hy-

drogen trapping effect is high enough, shear band activity is triggered, and the hydrogen induced internal shearing failure mode occurs. In the high stress triaxiality regime, the internal necking failure mode always dominates. Unlike the internal necking failure which results in an obviously enlarged void, the internal shearing failure could occur with only minor increase in the void volume fraction, which could possibly give a fracture surface with small or even indistinguishable dimples. These conclusions could be qualitatively related to the experimental observations reported by Matsuo et al. [17] and Matsuo et al. [25].

A hydrogen induced internal shearing failure criterion is proposed, defining the failure event as the formation of a "complete"shear band that links the void surface and the cell boundary. Considering that the shear band is featured by an obvious discontinuity in the rate of deformation field, its formation can be detected by observing the plastic stain rate histories. This criterion has been validated against the shear band formation criterion used by Li and Wierzbicki [42] for the plane strain tension situation and by relating the predicted internal shearing failure point to the sudden loss of the load bearing capacity of the unit cell.

The hydrogen failure loci are presented and discussed. Hydrogen enhanced internal necking failure is observed over the entire locus for a low level of hydrogen trapping effect. When the level of trapping effect is high, the failure locus consists of two branches, the internal shearing failure branch in the low stress triaxiality regime and the internal necking failure branch in the high triaxiality regime, and the intersection of these two branches is defined as the failure mode conversion point which signifies the transition from internal shearing to internal necking. While the internal necking failure branch maintains similar stress triaxiality dependence as in the absence of hydrogen, the internal shearing failure branch lowers only slightly with increase of stress triaxiality in the axisymmetric situation and could approximately be taken as triaxiality independent. A higher level of hydrogen trapping effect or a larger steepness of softening effect could postpone the failure mode conversion point and shift the internal shearing failure branch downward, however, the influence of hydrogen trapping on the internal necking failure branch is minor, indicating that the effect of trapped hydrogen on hydrogen enhanced internal necking failure in the high stress triaxiality regime is limited. The effect of Lode parameter on the internal shearing failure branch becomes more important in view that the triaxiality dependence is unpronounced. While the inter-

nal necking failure locus increases monotonically with the Lode parameter over the entire range $L \in (-1.0, 1.0)$, indicating that the axisymmetric tension is the most critical for hydrogen enhanced internal necking failure, the internal shearing failure locus decreases with the Lode parameter in the negative range $L \in (-1.0, 0.0)$ and increases in the positive range $L \in (0.0, 1.0)$, suggesting that the plane strain tension is the most critical for hydrogen induced internal shearing failure. This paper sheds new light on hydrogen-microvoid interactions at the continuum scale, and it paves the way for the future development of a microvoid process based hydrogen embrittlement assessment tool by providing micromechanical reference for establishing a proper hydrogen failure criterion.

Acknowledgements

The financial support from Aker Solutions and NTNU via the "Integrity of Ni-Alloys for Subsea Applications (INASA)"project is greatly acknowledged. We also want to thank the Research Council of Norway for funding through the "Hydrogen-induced degradation of offshore steels in ageing infrastructure - models for prevention and prediction (HIPP)". Contract No. 234130/E30.

Appendix A. Verification of the internal shearing failure criterion

The internal shearing failure point proposed in subsection 2.3 is easily distinguishable due to the uniqueness of the event at the formation of a "complete"shear band, and its effectiveness can be verified in two ways. The first is to compare the prediction of the new failure criterion to that of an existing one, and the one adopted by Li and Wierzbicki [42] is chosen for this purpose. As mentioned in subsection 2.3, the loss of positiveness of second order work of the continuum is a sufficient condition for material instability. By considering plain strain geometry with proportional loading, this condition is further simplified as $\frac{d\sigma_{flow}}{d\varepsilon_p} < 0$, which was used by Li and Wierzbicki [42] to detect the failure of a continuum element. In order to compare this criterion with our newly proposed one, a uniformly hydrogen pre-charged plane strain tensile specimen with the aforementioned sigmoidal hydrogen softening law and material $M3$ representing a high level of hydrogen trapping effect is considered. In order to trigger shear band localization during the numerical simulation, an initial perturbation in hydrogen concentration at the center of the specimen is applied,

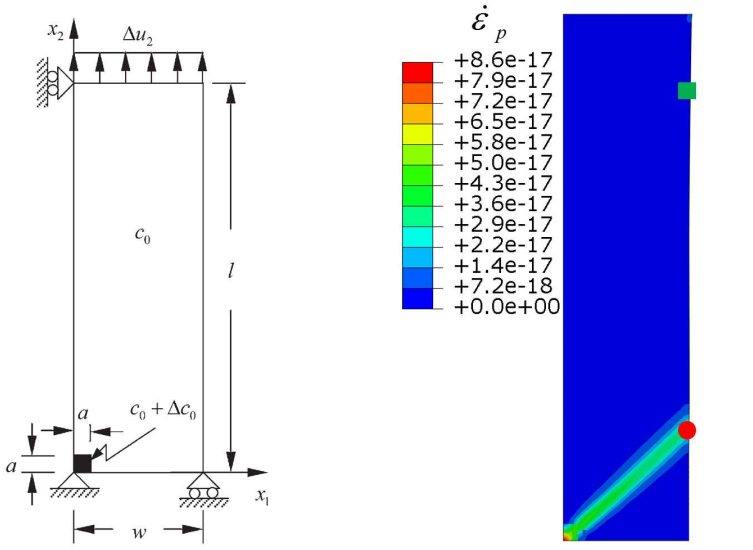

(a) Model illustration (b) Nominal strain $\varepsilon_n \approx 0.025$

Fig. A.21 (a) Illustration of the hydrogen pre-charged plane strain tensile specimen, only a quarter is shown due to symmetry [26]; (b) illustration of the "complete"shear band that spans over the entire width of the specimen.

as shown in Fig. A.21(a). Upon loading, a shear band emanates from the center of the specimen and extends towards the outer boundary until a "complete"shear band that spans over the entire width of the specimen is formed, as shown in Fig. A.21(b). More details regarding the numerical procedure and the development of the shear band can be found in Liang et al. [26]. In the finite element simulation using the damage model proposed by Li and Wierzbicki [42], material separation should initiate from the central element and propagate to the critical site which is the intersection point of the anticipated shear band and the specimen boundary, as marked by the circular dot in Fig. A.21(b). The history of the parameter, $\frac{d\sigma_{flow}}{d\varepsilon_p}$, that controls the element failure is plotted together with the nominal stress-strain curve of the specimen in Fig. A.22(a). It is observed that $\frac{d\sigma_{flow}}{d\varepsilon_p}$ is only negative in a narrow window of nominal strain, indicating that shear band instability is triggered in this regime and that the stable response is recovered in the post-initiation stage. Furthermore, it is noted that the occurrence of shear band instability corresponds very well to the sudden drop of the stress-strain curve which is the direct evidence for loss of bearing capacity, i.e. failure of the specimen. By far, the effectiveness of the criterion used by Li and Wierzbicki [42] in the hydrogen pre-charged plane strain tension situation has been re-verified. Subsequently,

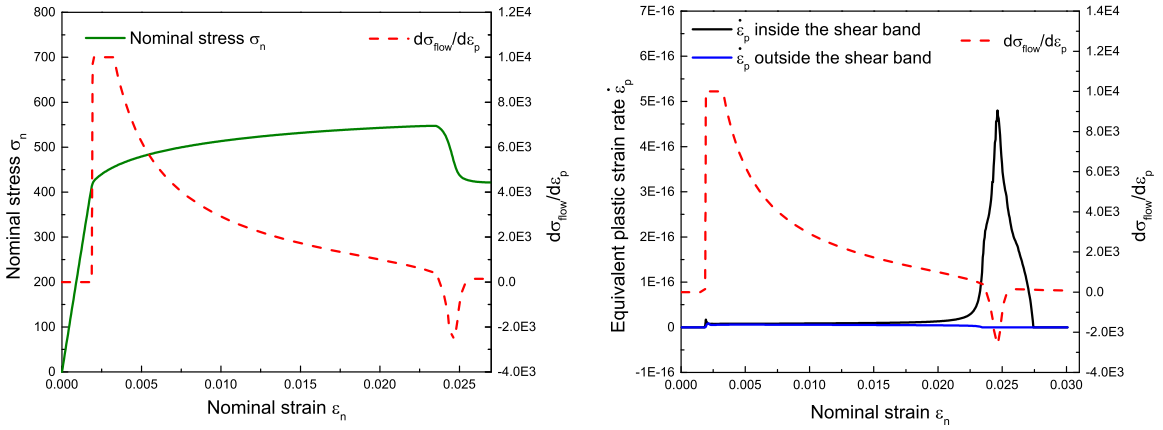

Fig. A.22 (*a*) The history of $\frac{d\sigma_{flow}}{d\varepsilon_p}$ at the critical site (circular dot in Fig. A.21(b)) and the nominal stress-strain curve indicating loss of loading bearing capacity; (*b*) comparison between the histories of $\dot{\varepsilon}_p$ and that of $\frac{d\sigma_{flow}}{d\varepsilon_p}$.

the histories of the plastic strain rate $\dot{\varepsilon}_p$ at the critical site and at a homogeneous deformation site (marked by the rectangular dot in Fig. A.21(b)) are plotted together with that of $\frac{d\sigma_{flow}}{d\varepsilon_p}$, as shown in Fig. A.22(b). Clearly, our newly proposed criterion, $\dot{\varepsilon}_p^b/\dot{\varepsilon}_p^o \rightarrow \infty$, predicts exactly the same shear band formation point as the $\frac{d\sigma_{flow}}{d\varepsilon_p}$ based criterion used by Li and Wierzbicki [42]. Therefore, the effectiveness of the newly proposed internal shearing failure criterion is validated in the plane strain situation. In fact, it is found to correspond well to the $\frac{d\sigma_{flow}}{d\varepsilon_p}$ based criterion in such situation.

Another way to verify the new failure criterion is to implement it directly to the unit cell analysis and to investigate the variation of the load bearing capacity of the cell. For such purpose, we take the cases of unit cell analyses with the sigmoidal hydrogen softening law with $k = 15$ at stress triaxiality $\eta = 1.0$ as an example. Two materials, $M1$ and $M3$, are investigated. As mentioned, hydrogen enhanced internal necking failure is observed in the case of $M1$ while hydrogen induced internal shearing failure is observe in the case of $M3$. The hydrogen enhanced internal necking failure point can be determined with the classical void coalescence criterion proposed by Koplik and Needleman [31] for unit cell analyses, and the hydrogen induced internal shearing failure is determined with the new failure criterion, i.e. failure initiation is associated with the peak point of the history of the $\dot{\varepsilon}_p$ ratio, as shown in Fig. 9(b). For material $M3$, it should be noted again that the unit cell simulation can go beyond the internal shearing failure point due to the lack of a

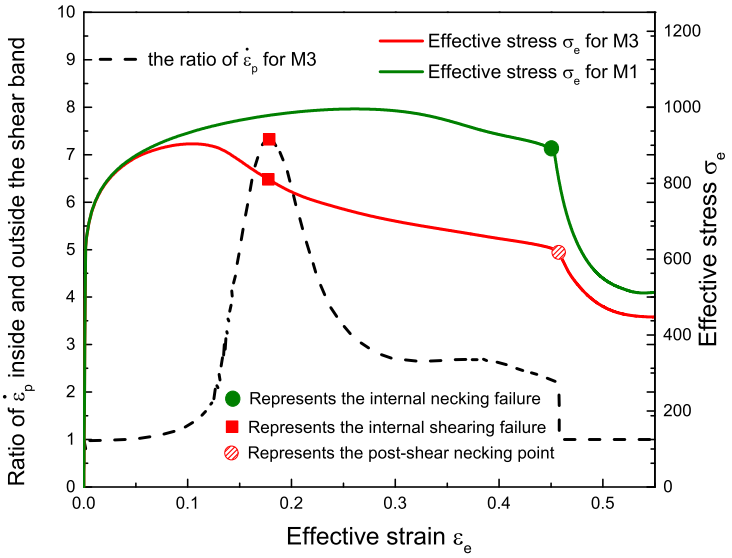

Fig. A.23 Illustration of the effective stress-strain curves for material $M1$ and $M3$ with the three points related to strain localization marked; the history of ratio of $\dot{\varepsilon}_p$ values inside and outside the shear band is also included. The stress triaxiality is $\eta = 1.0$.

material separation mechanism after shear localization, which will finally lead to the post-shear necking point. This event, as elaborated in subsection 3.1, is apparently artificial and cannot be defined as failure. In this case study, we can therefore detect three strain localization related points, i.e. the internal necking failure point in material $M1$, the internal shearing failure point and the post-shear necking point in material $M3$. These points are marked on the effective stress-strain curves obtained from the unit cell simulation, as shown in Fig. A.23. The history of ratio of $\dot{\varepsilon}_p$ values inside and outside the shear band is also included in this figure. Only one sudden drop in the effective stress-strain curve is observed in material $M1$, which corresponds exactly to the internal necking failure point. In material $M3$, however, two obvious drops of the curve are observed, corresponding to the internal shearing failure point and the post-shear necking point, respectively. Considering that the latter is artificial, the former should be taken as the realistic failure point, that is, the new failure criterion successfully predicts the hydrogen induced internal shearing failure in the unit cell analysis.

Appendix B. Mesh sensitivity of the internal shearing failure criterion

The mesh sensitivity is an important aspect for the implementation of the newly proposed internal shearing failure criterion in subsection 2.3. The mesh sensitivity roots in the local continuum theory which allows for an infinitely small band width at shear band localization, according to Benallal and Tvergaard [59]. After the shear band is initiated and upon further loading, the band width diminishes and, unless there is a physical limitation, it tends to zero [60]. At such point, unbounded shear strain values will be observed inside the infinitely thin band, indicating infinitely large discontinuity inside and outside the band. In the finite element simulation, the infinitely large discontinuity will have to be "smeared"across the maximum possible resolution of the mesh, i.e. one element, which yields a shear band with a finite width and a finite level of discontinuity. Apparently, with increasing mesh density, the numerical shear band will keep approaching the theoretical one which is infinitely thin with infinite discontinuity inside. Therefore, there exists no limiting mesh density where the numerical solution of the shear band localization converges. To eliminate such problem, the so-called nonlocal continuum theory, such as the strain gradient plasticity theory [61] with an internal length scale, needs to be introduced, which improves the situation but also poses new theoretical and computational difficulties at the same time [60]. In the present work, the local continuum theory with the intrinsic mesh sensitivity problem is adopted. While it may not give the exact absolute values of the discontinuity ($\dot{\varepsilon}_p$) inside the shear band, the failure point which is determined at the peak of the $\dot{\varepsilon}_p$ history according to the internal shearing failure criterion is found to converge when the mesh is fine enough, as shown by a mesh sensitivity study.

The mesh sensitivity study is performed via comparison of the results yielded by three cases with different mesh densities. The unit cell model is meshed in the same pattern as shown in Fig. 2(a), which guarantees the same ratio between the maximum and the minimum element sizes. Apparently, the maximum element size is found at the cell boundaries, and it is denoted L_b. The ratio between the cell boundary element size and the initial cell radius L_b/R_0 is then inversely proportional to the mesh density. The first case selected has $L_b/R_0 = 0.067$ which corresponds to a coarse mesh with $N_e = 1080$, with N_e denoting the total number of elements; the second case

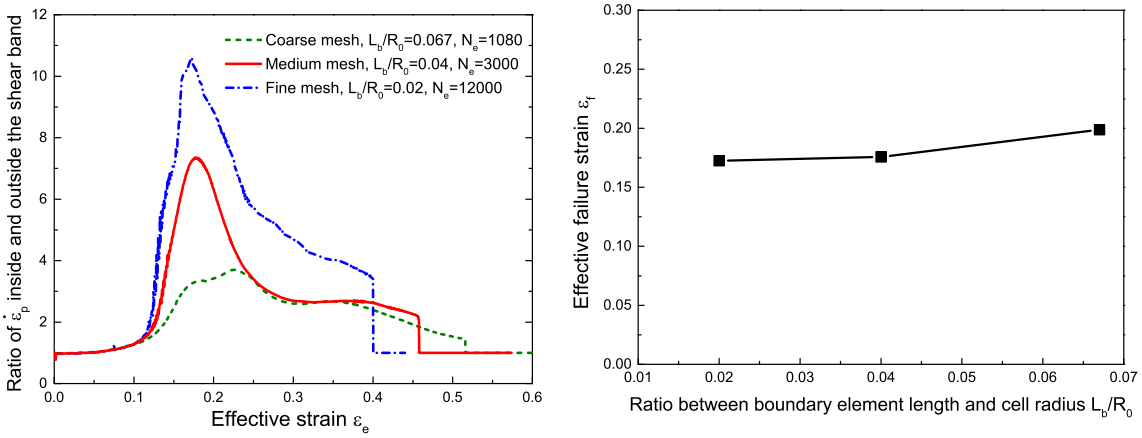

Fig. B.24 Effects of mesh density on (*a*) the history of ratio between $\dot{\varepsilon}_p$ values inside and outside the shear band and (b) the effective internal shearing failure strain. The material is $M3$ and the stress triaxiality is $\eta = 0.7$.

has $L_b/R_0 = 0.04$ which corresponds to a medium mesh with $N_e = 3000$, and the third case has $L_b/R_0 = 0.02$ which corresponds to a fine mesh with $N_e = 12000$. In all these cases, the coupled hydrogen diffusion-unit cell analyses are performed for material $M3$ at the sigmoidal hydrogen softening law with $k = 15$, and the constant stress triaxiality $\eta = 1.0$ is applied. The histories of the plastic strain rate ratio at the intersection of the anticipated shear band and the cell boundary are recorded and compared in Fig. B.24(a). In all the three cases, the plastic strain rate ratio at the observation site experiences a sudden increase followed by a decrease thereby giving a peak value, which according to the internal shearing failure criterion, signifies the formation of a "complete"shear band and is therefore defined as the internal shearing failure point. Meanwhile, the peak value is larger and more distinguishable with a finer mesh, which, according to the previous paragraph, can be attributed to the higher resolution of the $\dot{\varepsilon}_p$ field. While the peak in the case with the coarse mesh is almost unrecognizable, those in the cases with medium and fine mesh are easily distinguishable. Therefore, both cases with medium and fine mesh are applicable for the purpose of determining a clear failure point. The effective internal shearing failure strain values ε_f are then subtracted at the peak points and plotted against L_b/R_0 in Fig. B.24(b). The ε_f prediction seems only slightly mesh sensitive although the absolute value of $\dot{\varepsilon}_p$ is highly dependent on the mesh density as shown in Fig. B.24(a). It is only slightly overestimated in the case with a coarse mesh

and tends to converge in the cases with medium and fine mesh. We can therefore conclude that the newly proposed internal shearing failure criterion converges as long as the mesh is fine enough, since it is the ε_f prediction rather than the $\dot{\varepsilon}_p$ value that is of interest in this work. In addition, the hydrogen-microvoid interactions are investigated by the comparative study of the failure loci obtained with the same mesh at different conditions, and the influence of mesh sensitivity is therefore further removed. The case with medium mesh is adopted throughout the subsequent study, which yields distinguishable and accurate failure point as well as high computational efficiency.

References

[1] V. Olden, A. Alvaro, O. M. Akselsen, Hydrogen diffusion and hydrogen influenced critical stress intensity in an api x70 pipeline steel welded joint – experiments and fe simulations, International Journal of Hydrogen Energy 37 (15) (2012) 11474–11486.

[2] A. Alvaro, V. Olden, O. M. Akselsen, 3d cohesive modelling of hydrogen embrittlement in the heat affected zone of an x70 pipeline steel, International Journal of Hydrogen Energy 38 (18) (2013) 7539–7549.

[3] R. A. Oriani, A mechanistic theory of hydrogen embrittlement of steels, Berichte der Bunsengesellschaft für physikalische Chemie 76 (8) (1972) 848–857.

[4] H. K. Birnbaum, P. Sofronis, Hydrogen-enhanced localized plasticity—a mechanism for hydrogen-related fracture, Materials Science and Engineering: A 176 (1) (1994) 191–202.

[5] S. Lynch, Hydrogen embrittlement phenomena and mechanisms, Corrosion Reviews 30 (3-4) (2012) 105.

[6] H. Yu, J. S. Olsen, A. Alvaro, V. Olden, J. He, Z. Zhang, A uniform hydrogen degradation law for high strength steels, Engineering Fracture Mechanics 157 (2016) 56–71.

[7] P. Sofronis, Y. Liang, N. Aravas, Hydrogen induced shear localization of the plastic flow in metals and alloys, European Journal of Mechanics - A/Solids 20 (6) (2001) 857–872.

[8] H. K. Birnbaum, Hydrogen effects on deformation — relation between dislocation behavior and the macroscopic stress-strain behavior, Scripta Metallurgica et Materialia 31 (2) (1994) 149–153.

[9] I. M. Robertson, The effect of hydrogen on dislocation dynamics, Engineering Fracture Mechanics 68 (6) (2001) 671–692.

[10] Z. L. Zhang, C. Thaulow, J. Ødegård, A complete gurson model approach for ductile fracture, Engineering Fracture Mechanics 67 (2) (2000) 155–168.

[11] Z. L. Zhang, E. Niemi, Studies on the ductility predictions by different local failure criteria, Engineering Fracture Mechanics 48 (4) (1994) 529–540.

[12] A. Pineau, A. A. Benzerga, T. Pardoen, Failure of metals I: Brittle and ductile fracture, Acta Materialia 107 (2016) 424–483.

[13] A. Weck, D. S. Wilkinson, Experimental investigation of void coalescence in metallic sheets containing laser drilled holes, Acta Materialia 56 (8) (2008) 1774–1784.

[14] R. Garber, I. M. Bernstein, A. W. Thompson, Effect of hydrogen on ductile fracture of spheroidized steel, Scripta Metallurgica 10 (4) (1976) 341–345.

[15] R. Garber, I. M. Bernstein, A. W. Thompson, Hydrogen assisted ductile fracture of spheroidized carbon steels, Metallurgical Transactions A 12 (2) (1981) 225–234.

[16] H. Cialone, R. J. Asaro, The role of hydrogen in the ductile fracture of plain carbon steels, Metallurgical Transactions A 10 (3) (1979) 367–375.

[17] T. Matsuo, N. Homma, S. Matsuoka, Y. Murakami, Effect of hydrogen and prestrain on tensile properties of carbon steel SGP (0.078 C-0.012 Si-0.35 Mn, mass%) for 0.1 Mpa hydrogen pipelines, Transactions of the Japan Society of Mechanical Engineers Series A 74 (744) (2008) 1164–1173.

[18] T. Lee, T. Goldenberg, J. Hirth, Hydrogen and plastic instability in deformed spheroidized 1090 steel, in: ICF4, Waterloo (Canada) 1977, 1977.

[19] T. D. Lee, T. Goldenberg, J. P. Hirth, Effect of hydrogen on fracture of U-notched bend specimens of spheroidized AISI 1095 steel, Metallurgical Transactions A 10 (2) (1979) 199–208.

[20] O. A. Onyewuenyi, J. P. Hirth, Effects of hydrogen on notch ductility and fracture in spheroidized AISI 1090 steel, Metallurgical Transactions A 14 (1) (1983) 259–269.

[21] F. Yunchang, D. A. Koss, The influence of multiaxial states of stress on the hydrogen embrittlement of zirconium alloy sheet, Metallurgical Transactions A 16 (4) (1985) 675–681.

[22] B. P. Somerday, M. Dadfarnia, D. K. Balch, K. A. Nibur, C. H. Cadden, P. Sofronis, Hydrogen-assisted crack propagation in austenitic stainless steel fusion welds, Metallurgical and Materials Transactions A 40 (10) (2009) 2350–2362.

[23] I.-G. Park, A. W. Thompson, Hydrogen-assisted ductile fracture in spheroidized 1520 steel: Part I. axisymmetric tension, Metallurgical Transactions A 21 (1) (1990) 465–477.

[24] I.-G. Park, A. W. Thompson, Ductile fracture in spheroidized 1520 steel, Acta Metallurgica 36 (7) (1988) 1653–1664.

[25] T. Matsuo, J. Yamabe, S. Matsuoka, Effects of hydrogen on tensile properties and fracture surface morphologies of Type 316L stainless steel, International Journal of Hydrogen Energy 39 (7) (2014) 3542–3551.

[26] Y. Liang, P. Sofronis, N. Aravas, On the effect of hydrogen on plastic instabilities in metals, Acta Materialia 51 (9) (2003) 2717–2730.

[27] J. W. Rudnicki, J. R. Rice, Conditions for the localization of deformation in pressure-sensitive dilatant materials, Journal of the Mechanics and Physics of Solids 23 (6) (1975) 371–394.

[28] O. Barrera, E. Tarleton, H. W. Tang, A. C. F. Cocks, Modelling the coupling between hydrogen diffusion and the mechanical behaviour of metals, Computational Materials Science 122 (2016) 219–228.

[29] A. Premono, L. Liu, R. Miresmaeili, H. Kanayama, Finite element simulation of tensile tests for α iron in the presence of hydrogen, Journal of Computational Science and Technology 6 (2) (2012) 39–53.

[30] A. Premono, H. Kanayama, Characterization of void coalescence in Alpha-iron in the presence of hydrogen, Journal of Computational Science and Technology 7 (3) (2013) 395–409.

[31] J. Koplik, A. Needleman, Void growth and coalescence in porous plastic solids, International Journal of Solids and Structures 24 (8) (1988) 835–853.

[32] H. Yu, J. S. Olsen, J. He, Z. Zhang, Effects of loading path on the fracture loci in a 3D space, Engineering Fracture Mechanics 151 (2016) 22–36.

[33] D. C. Ahn, P. Sofronis, R. H. Dodds Jr, On hydrogen-induced plastic flow localization during void growth and coalescence, International Journal of Hydrogen Energy 32 (16) (2007) 3734–3742.

[34] Y. Liang, D. C. Ahn, P. Sofronis, R. H. Dodds Jr, D. Bammann, Effect of hydrogen trapping on void growth and coalescence in metals and alloys, Mechanics of Materials 40 (3) (2008) 115–132.

[35] Y. Liang, P. Sofronis, R. H. Dodds Jr, Interaction of hydrogen with crack-tip plasticity: effects of constraint on void growth, Materials Science and Engineering: A 366 (2) (2004) 397–411.

[36] H. Yu, J. S. Olsen, V. Olden, A. Alvaro, J. He, Z. Zhang, Cohesive zone simulation of grain size and misorientation effects on hydrogen embrittlement in nickel, Engineering Failure Analysis 81 (2017) 79–93.

[37] M. Dunand, D. Mohr, Effect of Lode parameter on plastic flow localization after proportional loading at low stress triaxialities, Journal of the Mechanics and Physics of Solids 66 (0) 133–153.

[38] A. Needleman, V. Tvergaard, Analyses of plastic flow localization in metals, Applied Mechanics Reviews 45 (3S) (1992) S3–S18, 10.1115/1.3121390.

[39] I. Barsoum, J. Faleskog, Rupture mechanisms in combined tension and shear—micromechanics, International Journal of Solids and Structures 44 (17) (2007) 5481–5498.

[40] I. Barsoum, J. Faleskog, Micromechanical analysis on the influence of the Lode parameter on void growth and coalescence, International Journal of Solids and Structures 48 (6) (2011) 925–938.

[41] V. Tvergaard, Bifurcation into a localized mode from non-uniform periodic deformations around a periodic pattern of voids, Journal of the Mechanics and Physics of Solids 69 (0) (2014) 112–122.

[42] Y. Li, T. Wierzbicki, Prediction of plane strain fracture of AHSS sheets with post-initiation softening, International Journal of Solids and Structures 47 (17) (2010) 2316–2327.

[43] A. Díaz, J. M. Alegre, I. I. Cuesta, Coupled hydrogen diffusion simulation using a heat transfer analogy, International Journal of Mechanical Sciences 115–116 (2016) 360–369.

[44] P. Sofronis, R. M. McMeeking, Numerical analysis of hydrogen transport near a blunting crack tip, Journal of the Mechanics and Physics of Solids 37 (3) (1989) 317–350.

[45] R. A. Oriani, The diffusion and trapping of hydrogen in steel, Acta Metallurgica 18 (1) (1970) 147–157.

[46] L. Jemblie, V. Olden, O. Akselsen, A coupled diffusion and cohesive zone modelling approach for numerically

assessing hydrogen embrittlement of steel structures, International Journal of Hydrogen Energy in press.

[47] P. Novak, R. Yuan, B. P. Somerday, P. Sofronis, R. O. Ritchie, A statistical, physical-based, micro-mechanical model of hydrogen-induced intergranular fracture in steel, Journal of the Mechanics and Physics of Solids 58 (2) (2010) 206–226.

[48] C. Ayas, V. S. Deshpande, N. A. Fleck, A fracture criterion for the notch strength of high strength steels in the presence of hydrogen, Journal of the Mechanics and Physics of Solids 63 (2014) 80–93.

[49] A. J. Kumnick, H. H. Johnson, Deep trapping states for hydrogen in deformed iron, Acta Metallurgica 28 (1) (1980) 33–39.

[50] Y. Yagodzinskyy, M. Ivanchenko, H. Hänninen, Hydrogen-dislocation interaction in austenitic stainless steel studied with mechanical loss spectroscopy, in: Solid State Phenomena, Vol. 184, Trans Tech Publ, 2012, pp. 227–232.

[51] M. Dadfarnia, M. L. Martin, A. Nagao, P. Sofronis, I. M. Robertson, Modeling hydrogen transport by dislocations, Journal of the Mechanics and Physics of Solids 78 (2015) 511–525.

[52] T. Zhang, W. Y. Chu, K. W. Gao, L. J. Qiao, Study of correlation between hydrogen-induced stress and hydrogen embrittlement, Materials Science and Engineering: A 347 (1–2) (2003) 291–299.

[53] S. Serebrinsky, E. A. Carter, M. Ortiz, A quantum-mechanically informed continuum model of hydrogen embrittlement, Journal of the Mechanics and Physics of Solids 52 (10) (2004) 2403–2430.

[54] A. Alvaro, V. Olden, O. M. Akselsen, 3d cohesive modelling of hydrogen embrittlement in the heat affected zone of an x70 pipeline steel – part ii, International Journal of Hydrogen Energy 39 (7) (2014) 3528–3541.

[55] R. Hill, A general theory of uniqueness and stability in elastic-plastic solids, Journal of the Mechanics and Physics of Solids 6 (3) (1958) 236–249.

[56] J. Kim, X. Gao, T. S. Srivatsan, Modeling of void growth in ductile solids: effects of stress triaxiality and initial porosity, Engineering Fracture Mechanics 71 (3) (2004) 379–400.

[57] X. Gao, J. Kim, Modeling of ductile fracture: Significance of void coalescence, International Journal of Solids and Structures 43 (20) (2006) 6277–6293.

[58] Y. Bai, T. Wierzbicki, A new model of metal plasticity and fracture with pressure and Lode dependence, International Journal of Plasticity 24 (6) (2008) 1071–1096.

[59] A. Benallal, V. Tvergaard, Nonlocal continuum effects on bifurcation in the plane strain tension-compression test, Journal of the Mechanics and Physics of Solids 43 (5) (1995) 741–770.

[60] M. Cervera, M. Chiumenti, C. Agelet de Saracibar, Shear band localization via local J2 continuum damage mechanics, Computer Methods in Applied Mechanics and Engineering 193 (9–11) (2004) 849–880.

[61] E. Martínez-Pañeda, C. F. Niordson, On fracture in finite strain gradient plasticity, International Journal of Plasticity 80 (2016) 154–167.